Vibration energy flow transmission in systems with Coulomb friction

Wei Dai[a, b], Jian Yang*[b], Marian Wiercigroch[c]

[a]*School of Naval Architecture and Ocean Engineering, Huazhong University of Science and Technology, Wuhan 430074, PR China*

[b]*Faculty of Science and Engineering, University of Nottingham Ningbo China, Ningbo 315100, PR China.*

[c]*Centre for Applied Dynamics Research, School of Engineering, Fraser Noble Building, King's College, University of Aberdeen, Aberdeen AB24 3UE, Scotland, UK*

Abstract

This study focusses on the vibration transmission and energy flow characteristics of low dimensional models of dynamical systems with Coulomb friction. The Karnopp friction model and smooth Coulomb friction models are employed to estimate the dry friction force. The steady-state responses of the system are determined by the harmonic balance (HB) approximations with numerical continuations and a time-marching method. The level of vibration transmission and energy dissipation within the system are assessed by the force transmissibility and power flow variables. For the single degree-of-freedom oscillator system, in the low- or high-frequency ranges away from the resonance, it is found that the dry frictional contact can suppress the vibration response and effectively dissipate vibrational energy. For the coupled oscillator, the existence of frictional contact at the interface can lead to a significant growth in the force transmissibility and energy transfer from the force-excited subsystem to the secondary system, especially at high excitation frequencies. The interfacial frictional contact can also result in a large amount of energy dissipation at the interface. The studies show that vibration transmission and energy dissipation in a dynamic system with contacting subsystems can be tailored by adjusting the properties of the frictional contact. Design strategies can be developed using frictional contacts for vibration suppression by minimizing vibration energy transmission or maximizing energy dissipation.

Keywords: vibration transmission; force transmissibility; energy dissipation; power flow analysis; Coulomb friction; nonlinear contact

1 Introduction

Engineering structures and systems often contain numerous parts or subsystems which are assembled in various ways. Friction can arise from the contacting surfaces of components subjected to relative motion, for example, in manipulator joints [1], drill-strings [2], disk brakes [3] and clutch structures [4]. Dry friction is usually undesirable due to the introduction of complexity associated with the nonlinear dynamics of the system. With the discontinuities introduced by frictions in the dynamic governing equations [5], engineering systems with friction can exhibit rich nonlinear phenomena [6, 7].

*Corresponding author: jian.yang@nottingham.edu.cn

In many applications, friction at a contact interface may cause unwanted effects to a system, such as frictional chatter [8], wear of components and noise due to the friction-related slipping [9]. On the other hand, in some applications, as in the case of the contact between the tyres of a vehicle and the road, friction can be necessary and useful. Given the energy dissipation effect, the friction within mechanical systems can be considered as a frictional damper, which consequently can be used to enhance the system performance for passive vibration control [10, 11].

To achieve an enhanced design of dynamical systems with contact interfaces, it is necessary to investigate the dynamics of systems with consideration of the influence of friction. For dynamic analysis of the engineering systems with dry friction nonlinearity, mass-spring models have been widely used in the past research. Some researchers investigated such systems under periodic loading. The classical work by Den Hartog [12] presented a piecewise analytical solution of the dynamic response for force-excited mass-spring systems based on the Coulomb damping model. Multiple-lockup characteristic of the mass for a certain time duration in each oscillation cycle was validated by experiment. Hundal [13] obtained the response of a single degree-of-freedom (DOF) Coulomb friction oscillator under base excitation. For the same base-excited mass-spring system, Marui and Kato [14] studied experimentally the stopping region of motion by placing a block mass excited by an eccentric cam and a ring spring on a flat-type guide with a rough surface. Marino and Cicirello [15] proposed an experimental framework for a single-DOF (SDOF) system under joined base-wall excitation and reported a design of a single-storey building set-up with a metal-to-metal contact. There were quite a few studies on friction-induced self-sustained vibration problems considering discrete SDOF or two-DOF (2DOF) coupled mass-spring systems placed on a continuously moving belt [16-18]. A pin-on-disc configuration was applied for experimental investigation of such systems [19]. Those mass-spring systems can exhibit stick-slip motion demonstrating strong influence of friction nonlinearity on the dynamic system responses.

A lot of previously reported work was focussed on the nonlinear dynamic analysis of forced systems with friction. Shaw [20] analysed a harmonically excited SDOF system with dry friction and determined the asymptotic stability. Aperiodic motions containing two distinct frequency components were found. Feeny [21] applied a qualitative technique to describe the dynamics of a forced multi-valued Coulomb friction oscillator and constructed the strange attractor for chaotic motion. Moreover, the geometric nature of the chaotic attractor was described using experimental Poincare maps by attaching a harmonically excited mass to the end of a cantilevered elastic beam [22]. Hong and Liu [23] investigated the dynamic motion of SDOF Coulomb friction oscillators subjected to harmonic loading and identified normal or abnormal zero-duration stop. Luo and Gegg [24] developed the force criteria for stick and non-stick motions in forced friction oscillators based on the local theory of non-smooth dynamical systems. Oancea and Laursen [25] explored experimentally the nature of transients entering and exiting stick phases in a forced mass-spring system with dry friction contact by using an elastic-mounted steel sphere sliding on a harmonically excited friction plate. Duan and Singh [26] studied a

2DOF torsional system with friction and found that the system can lose stability near the super-harmonic peak frequencies. Papangelo and Ciavarella [27] performed quasi-static analysis for a forced SDOF Coulomb frictional oscillator. Pascal [28] examined a linearly coupled 2DOF oscillator with one of the masses sliding on a rough surface and the friction force is characterized by Coulomb friction law. Several kinds of periodic orbits including one or more stops per cycles were observed. Sun *et al.* [29] established an extended energy balance method to predict the resonances for a forced SDOF system with friction contact from its nonlinear modes. Wiercigroch *et al.* [30] developed an experimental frictional oscillator consisting of a block mass moving along the guiding posts and a second mass with a vertical plate providing dry friction. With the use of such experimental rig, Wojewoda *et al.* [31] validated various qualitative nonlinear responses of a SDOF frictional oscillator. A novel experiment rig was further developed [32] to study the friction-related stick-slip nonlinear dynamic phenomena in the drill-bit rock interactions.

There has been a growing interest in the investigation of nonlinear friction damping for vibration attenuation purpose. Friction damping can be added as a connecting element in the adjacent engineering structures for vibration suppression purpose [33]. It also exists in the form of bolted joints [34]. The damping effect of friction has been considered for passive vibration control of turbine blades [35], machinery foundations and vehicles [36] and high-speed rotors [37]. The nonlinear dynamic behaviour of such systems and vibration suppression performance of the embedded friction damping have been studied [38]. Krack *et al.* [34] examined the nonlinear modal interactions in a jointed system induced by friction damping. It showed the possibility of taking advantage of friction damping to tune the system to obtain a minimum response level. The nonlinear vibration characteristics of bladed disks coupled by joints were analysed and it was shown that the friction damping within the joints may assist the vibration mitigation and improve the system integrity [39]. Claeys *et al.* [40] employed harmonic balance (HB) method to obtain the nonlinear vibration responses of a metallic assembly with friction damping under constant force input and conducted local analysis on the stick-slip behaviour in friction zone experimentally. Donmez *et al.* [41] revealed that the addition of friction damping to a quasi-zero stiffness (QZS) isolator can improve the isolation performance.

To achieve high performance vibration suppression of a built-up structure, it is important to establish comprehensive understanding on the mechanisms of vibration transmission through the nonlinear contacting interface and the energy dissipation at the interface of subsystems. In particular, the effects of the nonlinear friction contact on the vibration transmission and dissipation need to be investigated. Some researchers considered force transmissibility [42] and displacement transmissibility [33, 43] of SDOF mass-spring systems with friction damping. Ciğeroğlu and Özgüven [44] examined pseudo-receptance for the bladed disks with dry friction represented by lumped parameter model. Regarding the dissipative effect of friction, the friction damping at the connecting joint can largely affect the energy transfer and dissipation characteristics in the dynamical systems. However, much less work has been carried out on the vibration transmission of such systems from vibration energy flow

perspective. Lopez *et al.* [45] estimated the energy dissipation in a SDOF system with friction damper based on the classical Coulomb friction law and the theoretical results were validated by experiment [46]. Nicolas [47] numerically assessed the energy transfer via a friction-elastic-viscous link between a mass and a base with harmonic motion.

There is a limited number of investigations on energy transmission and dissipation in the coupled systems considering friction at the connecting interface [48]. The vibration power flow analysis (PFA) approach has been widely adopted as a tool for investigating the dynamic behaviour of coupled structures and complex systems. The power flow indices consider the combined effects of force and velocity amplitudes as well as their relative phase angle in a single concept, and thus can provide a qualitative measure of vibration energy transmission between subsystems and energy dissipation within an integrated dynamic system [49]. This approach has been used for the evaluation of vibration transmission in linear systems [50, 51]. In recent years, the PFA approach has been applied for investigating the dynamic behaviour of nonlinear systems [52-57] including non-smooth systems, such as bilinear systems and impact oscillators [58-60], from the energy flow viewpoint.

In this paper, the vibration energy flow transmission and dissipation characteristics of nonlinear non-smooth systems with frictional contact are investigated. The Coulomb frictional contact modelled by various approaches is considered to exist in a SDOF system and at the interface of coupled systems. The harmonic balance method with alternate-frequency-time (AFT) technique and numerical continuations are employed to investigate the vibration force transmission and power flow behaviour of systems with dry friction nonlinearity. Direct numerical integration is also conducted for comparison and validation of the analytical results. The effects of the nonlinear frictional contact on the dynamic responses, vibration transmission and energy dissipation characteristics are studied. The remaining content of this paper is organised as follows. Different Coulomb friction models and a general energy flow analysis framework for systems with friction are presented in Section 2. The dynamics and vibration transmission behaviour of the SDOF oscillator with dry friction is studied in Section 3. The influence of the frictional contact on the vibration energy transmission and dissipation at the interface of a coupled system is studied in Section 4. Conclusions are drawn at the end of the paper.

2 Energy flow analysis of systems with frictional contact

In this section, different models for the modelling of dry friction contact in dynamic systems are firstly introduced. These include the classical Coulomb friction model, the Karnopp model and the smooth approximation models using tanh-regularization approach or signum function approach. Using dry friction contact models, a general vibration energy flow analysis framework for the non-smooth systems with Coulomb friction is presented.

2.1 Dry friction contact models

Figure 1(a) shows a schematic of two contacting objects with masses m_a and m_b. Mass m_a is subjected to a constant force f_e in the horizontal direction. Normal and dry friction forces exist at the contact interface. Fig. 1(b) shows the classical Coulomb friction model, which is widely used to describe the relationship between the friction force f_c and the relative velocity v_r of the two objects. It shows that when there is relative motion between contact surfaces (i.e., the slip state), there exists dynamic friction force, with its direction opposite to that of the relative motion. When there is no relative motion between the contacting surfaces (i.e. the stick state), there may be static friction force counteracting the external force f_e.

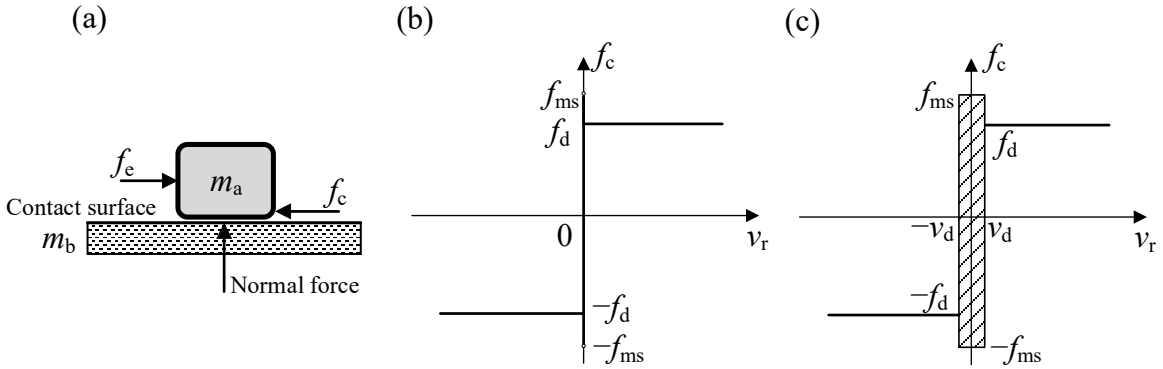

Figure 1. Schematic representation of (a) dry friction between two contacting solid bodies of m_a and m_b under resultant external force f_e in tangential direction; the relationship between friction force f_c and relative velocity v_r in (b) the classical Coulomb model and (c) the Karnopp model with magnitude of the dynamic friction force f_d and maximum static friction force f_{ms}. In (c), v_d is the boundary velocity of the dead zone for Karnopp model.

Mathematically, the classical Coulomb friction force can be expressed as

$$f_c = \begin{cases} f_d \operatorname{sgn}(v_r), & \text{if } v_r \neq 0, \\ f_{ms} \operatorname{sgn}(f_e), & \text{if } v_r = 0 \text{ and } |f_e| \geq f_{ms}, \\ f_e, & \text{if } v_r = 0 \text{ and } |f_e| < f_{ms}, \end{cases} \tag{1}$$

where f_d is the magnitude of the dynamic friction force, being the product of the coefficient of dynamic friction and the normal force, f_{ms} is the maximum static friction force, v_r is the relative velocity of the contacting objects, f_e is the resultant external force acting on a reference body in the tangential direction and $\operatorname{sgn}(v_r)$ is the signum function expressed by

$$\operatorname{sgn}(v_r) = \begin{cases} -1, & v_r < 0, \\ 0, & v_r = 0, \\ 1, & v_r > 0. \end{cases} \tag{2}$$

The classical Coulomb friction model introduces strong discontinuities at $v_r = 0$, which can create computational challenges for dynamic analysis. For instance, when applying a time-marching method to solve dynamic governing equations, the detection of $v_r = 0$ for switching friction state can yield inaccuracies due to the use of discrete and variable time steps. In this paper, a modified Coulomb friction model, the Karnopp model [61], is used in the numerical integration for determining the response of the systems with dry friction. As shown in Fig.1(c), compared to the classical Coulomb model, the Karnopp model assumes a small region of velocity dead zone $[-v_d, v_d]$, where the contact interface is considered

to be stuck and the relative velocity v_r is regarded null. In this way, some of the numerical issues encountered when using the classical Coulomb model can be avoided while the main characteristics of the friction model can still be captured. The Karnopp friction model is expressed as

$$f_\mathrm{c} = \begin{cases} f_\mathrm{d}\,\mathrm{sgn}(v_\mathrm{r}), & \text{if } |v_\mathrm{r}| > v_\mathrm{d}\,, \\ f_\mathrm{ms}\,\mathrm{sgn}(f_\mathrm{e})\,, & \text{if } |v_\mathrm{r}| \le v_\mathrm{d} \text{ and } |f_\mathrm{e}| \ge f_\mathrm{ms}\,, \\ f_\mathrm{e}\,, & \text{if } |v_\mathrm{r}| \le v_\mathrm{d} \text{ and } |f_\mathrm{e}| < f_\mathrm{ms}\,. \end{cases} \tag{3}$$

As in many applications $f_\mathrm{d} \approx f_\mathrm{ms}$, it is assumed that $f_\mathrm{d} = f_\mathrm{ms}$ throughout the paper.

The classical Coulomb friction force model contains discontinuities at $v_\mathrm{r} = 0$. It can be approximated by using smooth functions to facilitate dynamic analysis of systems with friction employing analytical or semi-analytical approaches based on the HB method [62]. One way is to use a smooth regularized hyperbolic tangent curve to approximate the friction force:

$$f_\mathrm{c} = f_\mathrm{d}\tanh(v_\mathrm{r}/\varepsilon) = f_\mathrm{d}\frac{\exp(v_\mathrm{r}/\varepsilon)-\exp(-v_\mathrm{r}/\varepsilon)}{\exp(v_\mathrm{r}/\varepsilon)+\exp(-v_\mathrm{r}/\varepsilon)}, \tag{4}$$

where ε is the tolerance parameter of the tanh-regularization. This tanh-regularization approach can eliminate the need for detection of stick-slip state transitions [63] and therefore the computational cost associated with dynamic analysis can be reduced.

Note that for dry friction modelling following the macro-slip approach, the Coulomb friction force is approximated by $f_\mathrm{c} \approx f_\mathrm{d}\mathrm{sgn}(v_\mathrm{r})$ and this can be named as the signum function approach [64]. For periodic responses with the relative velocity $v_\mathrm{r} \approx \sum_{k=1}^{N_\mathrm{H}}(\hat{v}_\mathrm{s}\sin(k\omega t) + \hat{v}_\mathrm{c}\cos(k\omega t))$, the friction force will be a periodic square wave and can be approximated using a smooth function based on Fourier series:

$$f_\mathrm{c} \approx \sum_{k=1}^{\infty} a_k\cos(k\omega t) + \sum_{k=1}^{\infty} b_k\sin(k\omega t). \tag{5}$$

where $a_k = \frac{\omega}{\pi}\int_0^{\frac{2\pi}{\omega}} f_\mathrm{d}\mathrm{sgn}(v_\mathrm{r})\cos(k\omega t)\,\mathrm{d}t$ and $b_k = \frac{\omega}{\pi}\int_0^{\frac{2\pi}{\omega}} f_\mathrm{d}\mathrm{sgn}(v_\mathrm{r})\sin(k\omega t)\,\mathrm{d}t$. As the signum function is an odd function, a_k should all be zero. For instance, when $v_\mathrm{r} \approx \hat{v}_\mathrm{s}\sin(\omega t)$, the friction force can be approximated by using a fifth order Fourier expansion as

$$f_\mathrm{c} \approx \frac{4f_\mathrm{d}}{\pi}\left(\sin(\omega t) + \frac{1}{3}\sin(3\omega t) + \frac{1}{5}\sin(5\omega t)\right). \tag{6}$$

Figures 2(a) and (b) show two ways of smoothing and approximating the Coulomb friction force, which are named as the tanh-regularization approach and the Fourier series expansion of the signum function approach, respectively. In Fig. 2(a), the magnitudes of the dynamic and static friction forces for those four cases are set as $f_\mathrm{d} = f_\mathrm{ms} = 0.06$ and the tolerance parameter ε changes from 0.1 to 0.2 and to 0.3. It is shown that a smaller value of ε can provide a better approximation of the friction force based on the classical Coulomb model. Fig. 2(b) presents the time histories of the Coulomb friction force represented by using the Fourier series approximations of the signum function. It shows that the first-order Fourier expansion can provide a rough approximation to the Coulomb friction force. As the number of the Fourier terms increases to 3, the wave form of the Coulomb friction force can be better captured and approximated. By further increasing the Fourier terms, the square wave force can be almost completely represented. In this paper, the Fourier series expansion of the signum function

approach is used in the analytical derivation of the frequency-response relationship to gain physical insights of the system dynamics. The tanh-regularization approach is used in the semi-analytical HB approximations of the steady-state responses. To ensure the accuracy of the truncation when using the Fourier expansion, the original time domain expression of the friction force is also used for the determination of the dynamic response using the time marching method.

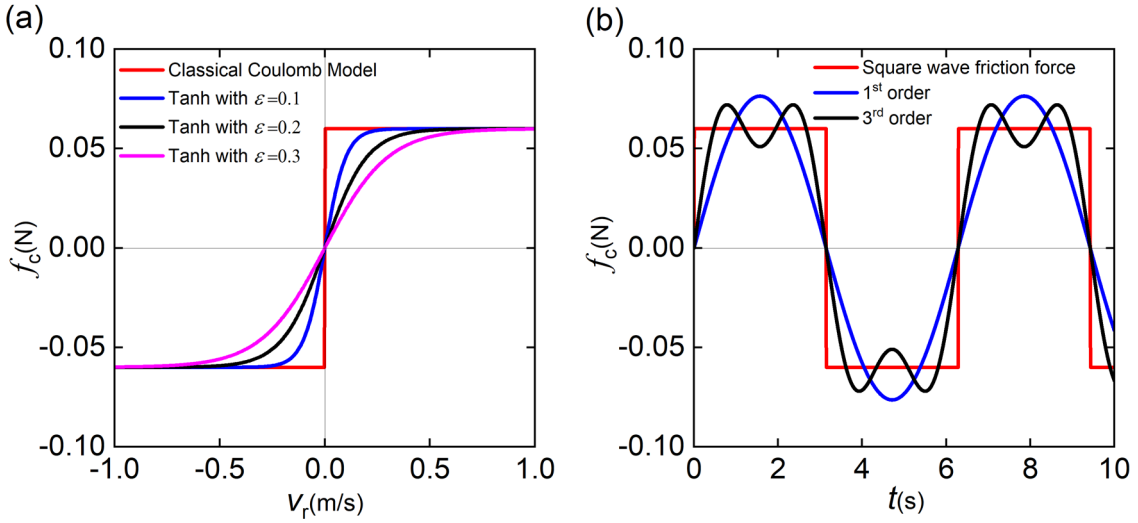

Figure 2. Smoothing the Coulomb friction force f_c by (a) the tanh-regularization approach and (b) the Fourier series expansion of the signum function approach. In (a), the red line is for the classical Coulomb friction model, the blue, black and pink lines are for regularized hyperbolic tangent curves with $\varepsilon = 0.1$, 0.2 and 0.3, respectively. In (b), the red colour marks the square wave Coulomb friction force. The blue and black curves are for its 1st order and 3rd order Fourier series representations.

2.2 Energy flow formulations

For a general Q-DOF chain oscillator system with friction at coupling interfaces, the dimensionless equation of motion and the energy flow balance equation can be expressed in a matrix form as

$$\mathbf{M}\mathbf{X}'' + \mathbf{C}\mathbf{X}' + \mathbf{K}\mathbf{X} + \mathbf{F}_c\left(\Delta(\mathbf{X}')\right) = \mathbf{F}_{ef}(\tau), \tag{7a}$$

$$\mathbf{X}'^{\mathrm{T}}\mathbf{M}\mathbf{X}'' + \mathbf{X}'^{\mathrm{T}}\mathbf{C}\mathbf{X}' + \mathbf{X}'^{\mathrm{T}}\mathbf{K}\mathbf{X} + \mathbf{X}'^{\mathrm{T}}\mathbf{F}_c\left(\Delta(\mathbf{X}')\right) = \mathbf{X}'^{\mathrm{T}}\mathbf{F}_{ef}(\tau), \tag{7b}$$

respectively, where $\mathbf{X}$, $\mathbf{X}'$ and $\mathbf{X}''$ denote the displacement, velocity and acceleration vectors, respectively, $\mathbf{M}$, $\mathbf{C}$ and $\mathbf{K}$ are the mass, damping and stiffness matrices, respectively, $\mathbf{F}_c\left(\Delta(\mathbf{X}')\right)$ is the dimensionless nonlinear friction force induced by frictional contact and $\Delta(\mathbf{X}')$ is the relative velocity between the two contacting masses, $\mathbf{F}_{ef}(\tau)$ represents harmonic force excitation applied to the q-th DOF $(1 \le q \le Q)$ of the system with $\mathbf{F}_{ef}(\tau) = \{\ldots, \ F_0 e^{i\Omega\tau}, \ \ldots\}^{\mathrm{T}}$, of which F_0 and Ω are the non-dimensional force amplitude and excitation frequency, respectively, and τ is the dimensionless time.

For the numerical determination of the steady-state response of the system, the nonlinear friction force $\mathbf{F}_c\left(\Delta(\mathbf{X}')\right)$ in Eq. (7) can be firstly modelled by the Karnopp model. Eq. (7a) can then be solved by the adaptive Runge-Kutta (RK) Dormand-Prince method with variable step size. The energy dissipation and the force transmission between sub-systems can be determined subsequently. For the implementation of the Runge-Kutta method, a fourth-order and a fifth-order approximations from one point to the next point are calculated and compared. An optimum step size is then obtained to reduce

the total computing time while the estimated error in each step is ensured to be smaller than the tolerance. In the treatment of the non-smooth friction force term in the governing equation, conditional execution statements are made in the numerical algorithm to capture the existence of discontinuities in the friction force based on the Karnopp model. It should be mentioned that the Karnopp model may be more efficient and accurate than the classical Coulomb model from numerical aspects. However, the resultant external force applied to the contact interface, which is needed in the Karnopp model, may be difficult to define in the multi-DOF system (i.e. $Q > 2$) [62].

As for comparisons, the semi-analytical harmonic balance approximation method is also used for obtaining the steady-state periodic response of the system with dry friction. Here the dry friction force $\mathbf{F}_{\mathrm{c}}\left(\Delta(\mathbf{X}')\right)$ in Eq. (7) can be modelled by the tanh-regularization approach considering the friction force as a continuous and differentiable function of the relative velocity. The steady-state displacement response $\mathbf{X}$ and the nonlinear friction force $\mathbf{F}_{\mathrm{c}}\left(\Delta(\mathbf{X}')\right)$ can be approximated by a truncated N-order Fourier series with a fundamental frequency of Ω:

$$\mathbf{X} = \left\{\sum_{n=0}^{N} \tilde{R}_{(1,n)}\, \mathrm{e}^{\mathrm{i}n\Omega\tau}, \quad \ldots \quad \sum_{n=0}^{N} \tilde{R}_{(q,n)}\, \mathrm{e}^{\mathrm{i}n\Omega\tau}, \quad \ldots \quad \sum_{n=0}^{N} \tilde{R}_{(Q,n)}\, \mathrm{e}^{\mathrm{i}n\Omega\tau}\right\}^{\mathrm{T}}, \tag{8a}$$

$$\mathbf{F}_{\mathrm{c}}\left(\Delta(\mathbf{X}')\right) = \left\{\sum_{n=0}^{N} \tilde{H}_{(1,n)}\, \mathrm{e}^{\mathrm{i}n\Omega\tau}, \quad \ldots \quad \sum_{n=0}^{N} \tilde{H}_{(q,n)}\, \mathrm{e}^{\mathrm{i}n\Omega\tau}, \quad \ldots \quad \sum_{n=0}^{N} \tilde{H}_{(Q,n)}\, \mathrm{e}^{\mathrm{i}n\Omega\tau}\right\}^{\mathrm{T}}, \tag{8b}$$

respectively, where $\tilde{R}_{(q,n)}$ and $\tilde{H}_{(q,n)}$ are the complex Fourier coefficients of the n-th order Fourier approximation corresponding to the q-th DOF, $\mathbf{X}'$ and $\mathbf{X}''$ can then be obtained by differentiating the displacement $\mathbf{X}$ with respect to time τ. To determine the Fourier coefficients $\tilde{H}$ of the nonlinear friction force $\mathbf{F}_{\mathrm{c}}\left(\Delta(\mathbf{X}')\right)$ in Eq. (8b), the AFT technique can be used, which has been widely applied for the treatment of nonlinear forces in the analysis of nonlinear dynamical systems [65]. The basic idea of the AFT scheme is to substitute the expressions of the approximated harmonic responses of $\mathbf{X}$, $\mathbf{X}'$ and $\mathbf{X}''$ into the nonlinear force expression of $\mathbf{F}_{\mathrm{c}}\left(\Delta(\mathbf{X}')\right)$. The time histories of nonlinear friction force can be obtained and can then be Fourier transformed to find the Fourier coefficients $\tilde{H}$.

After the determination of the Fourier coefficients $\tilde{H}$, Eq. (8) can be substituted into the governing equation of Eq. (7a) and by balancing the corresponding coefficients of the n-th ($0 \le n \le N$) order harmonic terms of the resultant equation, we have

$$(-(n\Omega)^2\mathbf{M} + \mathrm{i}(n\Omega)\mathbf{C} + \mathbf{K})\tilde{\mathbf{R}}_n = \tilde{\mathbf{S}}_n - \tilde{\mathbf{H}}_n, \tag{9}$$

where $\tilde{\mathbf{R}}_n = \left\{\tilde{R}_{(1,n)}, \quad \ldots \quad \tilde{R}_{(q,n)}, \quad \ldots \quad \tilde{R}_{(Q,n)}\right\}^{\mathrm{T}}$, $\tilde{\mathbf{H}}_n = \left\{\tilde{H}_{(1,n)}, \quad \ldots \quad \tilde{H}_{(q,n)}, \quad \ldots \quad \tilde{H}_{(Q,n)}\right\}^{\mathrm{T}}$ and $\tilde{\mathbf{S}}_n = \{0, \quad \ldots \quad F_0, \quad \ldots \quad 0\}^{\mathrm{T}}$. By sorting N harmonic equations of Eq. (9), a set of real nonlinear algebraic equations with the total number of $Q(2N+1)$ can be obtained. The Newton-Raphson iterative method can be employed to solve those equations and an arc-length continuation method is also used to trace the solution path in the frequency domain [66]. Subsequently, the steady-state response of the system can be obtained. The level of force transmission and power flow behaviour within the oscillator system can then be evaluated.

Note that the value of N for the truncation of the Fourier expansion of the friction force should be carefully selected. A larger N used in high-order HB can yield a better representation of the nonlinear friction force, hence providing more accurate predictions of the steady-state responses. However, the computational cost increases quickly with N. Therefore, a sufficiently large value of N is used after validating the corresponding HB results using the numerical integration results to ensure the accuracy of truncation.

For the power flow analysis of the oscillator system with dry friction, the total instantaneous input vibration power into the system is the product of the harmonic excitation force $F_0 \mathrm{e}^{\mathrm{i}\Omega\tau}$ and the corresponding velocity X_q' of the q-th DOF. Note that the velocity X_q' can be obtained by taking differentiation of Eq. (8a) as $X_q' = \sum_{n=0}^{N} \mathrm{i}n\Omega\tilde{R}_{(q,n)}\, \mathrm{e}^{\mathrm{i}n\Omega\tau}$, hence we have

$$P_{\mathrm{in}} = \Re\{X_q'\}\Re\{F_0 e^{\mathrm{i}\Omega\tau}\} = \Re\{\textstyle\sum_{n=0}^{N} \mathrm{i}n\Omega\tilde{R}_{(q,n)}\, e^{\mathrm{i}n\Omega\tau}\}\Re\{F_0 e^{\mathrm{i}\Omega\tau}\}, \tag{10}$$

where the symbol $\Re$ represents the operation of taking the real part of a complex number. The steady-state time-averaged input vibration power into the system is

$$\bar{P}_{\mathrm{in}} = \frac{1}{\tau_{\mathrm{p}}}\int_{\tau_0}^{\tau_0+\tau_{\mathrm{p}}} P_{\mathrm{in}}\, \mathrm{d}\tau = \frac{1}{2}F_0\Re\{(\mathrm{i}\Omega\tilde{R}_{(q,1)})^*\}, \tag{11}$$

where τ_0 and τ_{p} are the starting time for averaging and the averaging time span, respectively, and in the current study, τ_{p} is set as one period of excitation with $\tau_{\mathrm{p}} = 2\pi/\Omega$, the symbol * denotes the mathematical operation of taking the complex conjugate of a complex number.

The maximum kinetic energy has been widely used as one of the performance indicators of vibration suppression systems [50]. For the current system, the non-dimensional maximum kinetic energy K_q for the q-th DOF is defined as

$$K_q = \frac{1}{2}(|X_q'|_{\max})^2, \tag{12}$$

where $|X_q'|_{\max}$ is the maximum magnitude of velocity for the q-th DOF in the steady-state response.

3 Single-DOF systems with dry friction contacts

In this section, the vibration energy transmission and dissipation characteristics of SDOF systems with dry friction are studied. Two SDOF systems comprising a vertical wall separated or jointed with the ground are firstly presented. Then the dynamic responses of the systems are obtained by the analytical, semi-analytical or direct numerical integration approaches based on different friction models. The force transmissibility and vibration energy dissipation within the system are formulated. Parametric studies of the influence of friction on the force transmission and vibration energy flow behaviour of the system are carried out.

3.1 Dynamic response analysis

Figures 3(a) and (b) show two SDOF systems comprising a mass m_1 connected to the ground via a viscous damper with damping coefficient c_1 and a linear spring with stiffness coefficient k_1. The mass

is also sliding on a vertical rough wall and the dry friction force f_c exists in the contact with the magnitude of f_d. The vertical wall is separated from the base ground in Fig. 3(a) while jointed with the base ground in Fig. 3(b). The mass is subjected to a harmonic force excitation with the forcing amplitude f_0 and frequency ω. The equilibrium position of the mass is set as the reference with $x_1 = 0$. The governing equation of the system is

$$m_1\ddot{x}_1 + c_1\dot{x}_1 + k_1x_1 + f_c = f_0\cos\omega t, \tag{13}$$

where f_c is the nonlinear dry friction force. When the Karnopp model is used, we have $v_r = \dot{x}_1$ and $f_e = f_0\cos\omega t - k_1x_1$ in Eq. (3). The following non-dimensional parameters and variables are introduced for our parametric studies:

$$\omega_1 = \sqrt{\frac{k_1}{m_1}}, \quad \zeta_1 = \frac{c_1}{2m_1\omega_1}, \quad X_1 = \frac{x_1}{l_0}, \quad F_d = \frac{f_d}{k_1l_0}, \quad \eta = \frac{\varepsilon}{\omega_1 l_0}, \tag{14a-14e}$$

$$V_d = \frac{v_d}{\omega_1 l_0}, \quad F_0 = \frac{f_0}{k_1l_0}, \quad \Omega = \frac{\omega}{\omega_1}, \quad \tau = \omega_1 t, \tag{14f-14i}$$

where ω_1 and ζ_1 are the undamped natural frequency and the damping ratio of the system without considering the friction, respectively, l_0 is the undeformed length of the linear spring at the bottom, X_1 is the dimensionless displacement of the mass, F_d is the non-dimensional magnitude of the dynamic dry friction force (which is named magnitude of friction hereafter), η is the ratio of tolerance parameter in the tanh-regularization approach and V_d is the dimensionless boundary velocity of the dead zone in the Karnopp model, F_0, Ω and τ are the non-dimensional excitation amplitude, excitation frequency and the dimensionless time, respectively. By using those defined parameters in Eq. (14), Eq. (13) can be transformed into its non-dimensional form described as

$$X_1'' + 2\zeta_1X_1' + X_1 + F_c = F_0\cos\Omega\tau, \tag{15}$$

where the prime denotes differentiation with respect to τ, and F_c is the non-dimensional friction force.

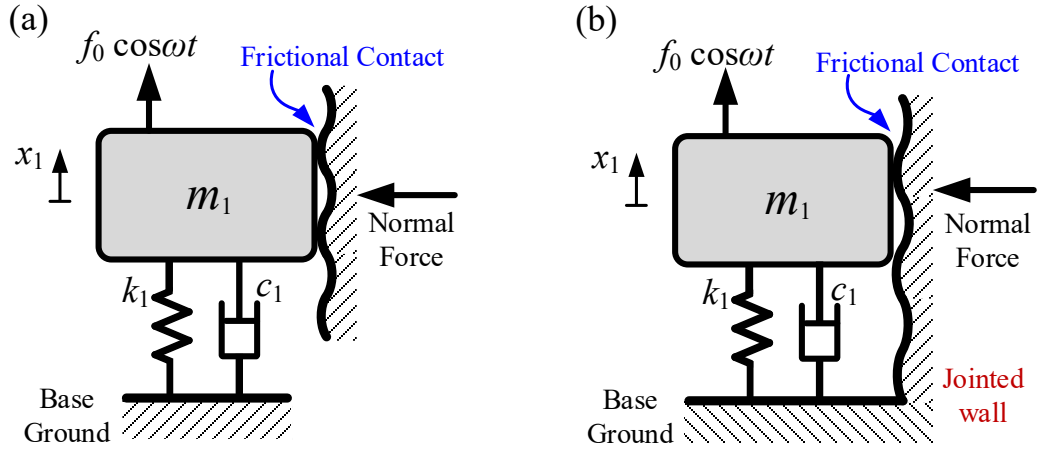

Figure 3. A generic harmonic excited SDOF mass-spring-damper system with (a) a vertical wall separated from the horizontal base and (b) a vertical wall jointed with the horizontal base. Coulomb frictional contact exists between the vertical wall and the vibrating mass.

To obtain analytical approximations of the frequency-response solution of Eq. (15), the steady-state periodic dimensionless response of the system is assumed to be

$$X_1 = R_0 + R_1\cos(\Omega\tau+\phi) = R_0 + R_1\cos\theta = R_1(\cos\theta - \cos\theta_0), \tag{16a}$$

$$X_1' = -\Omega R_1\sin(\Omega\tau+\phi) = -\Omega R_1\sin\theta,\ X_1'' = -\Omega^2 R_1\cos(\Omega\tau+\phi) = -\Omega^2 R_1\cos\theta, \tag{16b, 16c}$$

where $\theta = \Omega\tau+\phi$, $\theta_0 = \cos^{-1}(-R_0/R_1)$, R_0 and R_1 are the dimensionless displacement amplitudes for the static and fundamental frequency components, respectively. By using the signum function approach, the third order Fourier series expansion on the non-dimensional dry friction force F_c based on Eq. (6) is expressed as:

$$F_c \approx F_d\,\mathrm{sgn}(X_1') \approx -\frac{4}{\pi}\left(\sin\theta + \frac{1}{3}\sin 3\theta\right)F_d. \tag{17}$$

By inserting Eqs (16) and (17) into Eq. (15) and balancing the static term and the coefficients of the $\cos\theta$ and $\sin\theta$ terms, we obtain

$$R_0 = 0, \qquad (1-\Omega^2)R_1 = F_0\cos\phi, \qquad -2\Omega\zeta_1 R_1 - \frac{4}{\pi}F_d = F_0\sin\phi. \tag{18a, b, c}$$

By a manipulation of Eqs (18b) and (18c) in order to cancel out the trigonometric terms of ϕ, we obtain

$$(1-\Omega^2)^2R_1^2 + (2\Omega\zeta_1 R_1 + \frac{4}{\pi}F_d)^2 = F_0^2, \tag{19}$$

where R_1 is then obtained by solving the quadratic equation. Then the steady-state dimensionless response amplitude X_{1_amp} of the mass can be determined as

$$X_{1\_amp} = |R_1| = \frac{-8F_d + \sqrt{64F_d^2 - \{[16F_d^2 - \pi^2F_0^2][(1-\Omega^2)^2/(\Omega\zeta_1)^2+4]\}}}{\pi[(1-\Omega^2)^2/(\Omega\zeta_1)+4\Omega\zeta_1]}. \tag{20}$$

The HB-AFT scheme illustrated in Subsection 2.2 can also be used as a semi-analytical approximation method to obtain the steady-state response of the system governed by Eq. (15). For the implementation, the non-dimensional friction force is approximated by

$$F_c = F_d\frac{\exp(X_1'/\eta) - \exp(-X_1'/\eta)}{\exp(X_1'/\eta) + \exp(-X_1'/\eta)}, \tag{21}$$

based on the tanh-regularization representation from Eq. (4). For dynamic analysis using direct numerical integration based on the Runge-Kutta Dormand-Prince method. A variable step size is adopted while ensuring the estimated error is below a pre-defined value. The friction force F_c is expressed by

$$F_c = \begin{cases} F_d\,\mathrm{sgn}(X_1'), & \text{if } |X_1'| > V_d, \\ F_d\,\mathrm{sgn}(F_e), & \text{if } |X_1'| \le V_d \text{ and } |F_e| \ge F_d, \\ F_e, & \text{if } |X_1'| \le V_d \text{ and } |F_e| < F_d, \end{cases} \tag{22}$$

based on the Karnopp model from Eq. (3), where $F_e = F_0 e^{i\Omega\tau} - X_1$ is the non-dimensional resultant force applied to the contacting interface in the tangential direction.

In Fig. 4, the effects of dry friction on the steady-state response amplitude X_{1_amp} of the mass shown in Fig. 3 are investigated. Fig. 4(a) presents a comparison of X_{1_amp} results obtained by different approaches. The red and black lines represent the results obtained by the semi-analytical HB-AFT method for the linear frictionless system ($F_d = 0$) and the nonlinear system with frictional contact ($F_d = 0.04$), respectively. With a trade off between the accuracy and computational time, the order N used in HB-AFT approximations is set as 7 throughout the paper. The squares and rhombus denote the response

amplitude for the same nonlinear frictional system ($F_d = 0.04$) computed by the Runge-Kutta method with adaptive-step-size and the analytical HB method, respectively. When employing the Runge-Kutta method, the non-smoothness of the friction force is reflected by the conditional statement in the algorithm and the relative error tolerance is set as 10^{-6} throughout this paper. The other system parameters are fixed as $\zeta_1 = 0.01$, $V_d = 1 \times 10^{-4}$, $\eta = 1 \times 10^{-4}$ and $F_0 = 0.1$.

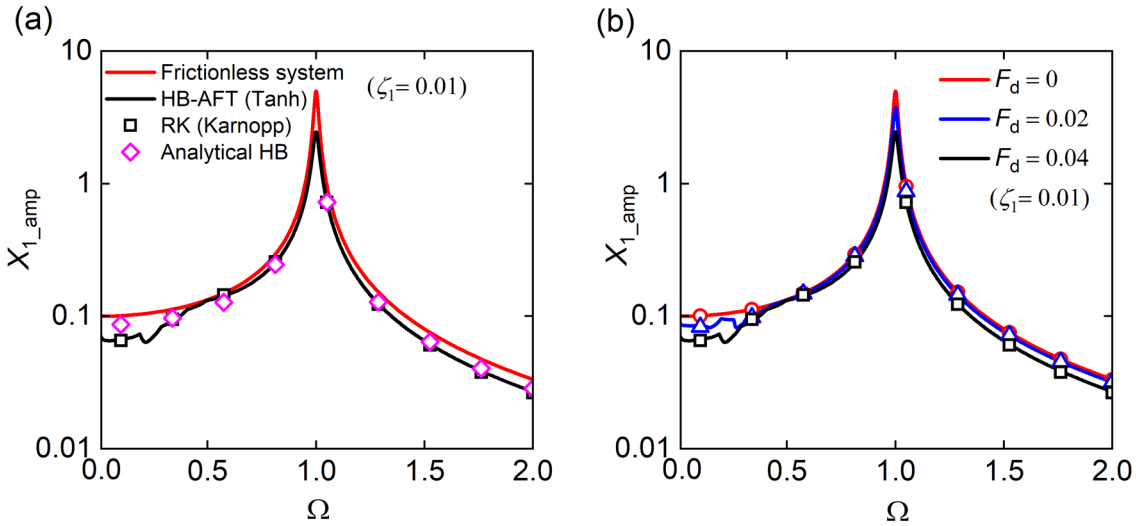

Figure 4. (a) Comparison of steady-state response solutions from HB-AFT, analytical HB and RK approaches, and (b) the effects of the magnitude of friction F_d on the steady-state response amplitude X_{1_amp}. In (a), the red and black lines are for the results obtained by the HB-AFT method with $F_d = 0$ and 0.04 respectively. The squares and rhombuses are for the results obtained by the RK method and analytical-HB method, respectively, with $F_d = 0.04$; In (b), the red, blue and black lines are for HB-AFT results with $F_d = 0$, 0.02 and 0.04, respectively. Circular, triangular and square symbols denote RK results.

Figure 4(a) shows that the analytical HB yields relatively accurate approximations of the responses when the excitation frequency is in the vicinity of the resonance. However, due to the relatively low number of Fourier terms used in the analytical HB, at low or high frequencies differences appear between the analytical and the numerical integration results. In comparison, the HB-AFT results agree well with the numerical results over the whole frequency range, demonstrating the accuracy of the truncation in Fourier expansion approximations. Therefore, for a better demonstration of the effects of the strong friction nonlinearity on the vibration transmission and energy dissipation, only the 7th order HB-AFT results and RK results are presented in the following content. Fig. 4(b) shows the effects of the presence of the dry friction on the system response, with the magnitude of friction F_d being 0, 0.02 and 0.04, respectively. The other parameters are set the same as those used in Fig. 4(a). The results obtained by the HB-AFT approximations are represented by different colours of lines, while those obtained by using the RK method are denoted by symbols. Fig. 4(b) shows that by comparing to the linear system with $F_d = \rho = 0$, the involvement of the dry friction contact between the mass and wall can suppress the vibration of the mass in a broad frequency band, demonstrated by reductions in steady-state response amplitude X_{1_amp}. It shows that as the magnitude of friction F_d increases from 0.02 to 0.04, there is a stronger suppression effect on the X_{1_amp} in a wide frequency range. Of contrast to the effects of dry friction on the response amplitude, it is well-documented that for a SDOF mass-spring-

damper linear system, an increase in the viscous damping ratio ζ_1 can lead to a substantial reduction in the peak response amplitude, but small changes in the response amplitude when away from the resonant frequency region. Fig. 4(b) indicates that a major difference in the effects of dry friction and viscous damping on the dynamic response and vibration suppression is the frequency range being affected.

Figure 5 presents the steady-state time histories of the responses, specifically the friction force F_c and the viscous damping force F_{cd} ($F_{cd} = 2\zeta_1 X_1'$) at particular frequencies in Fig. 4. The system with dry frictional contact is investigated by setting the magnitude of friction $F_d = 0.02$ in Fig. 5(a) and F_d=0.04 in Figs 5(b) and (c) while setting viscous damping ratio ζ_1 of the system to be 0.01. In Figs 5(d), (e) and (f), the linear system without dry friction ($F_d = 0$) is examined with $\zeta_1 = 0.01$ in Fig. 5(d) and $\zeta_1 = 0.03$ in Figs 5(e) and (f). Parameters are set as $V_d = 1 \times 10^{-4}$, $\eta = 1 \times 10^{-4}$ and $F_0 = 0.1$, the same as those used in Fig. 4. The results are obtained by using the RK method and the Karnopp model.

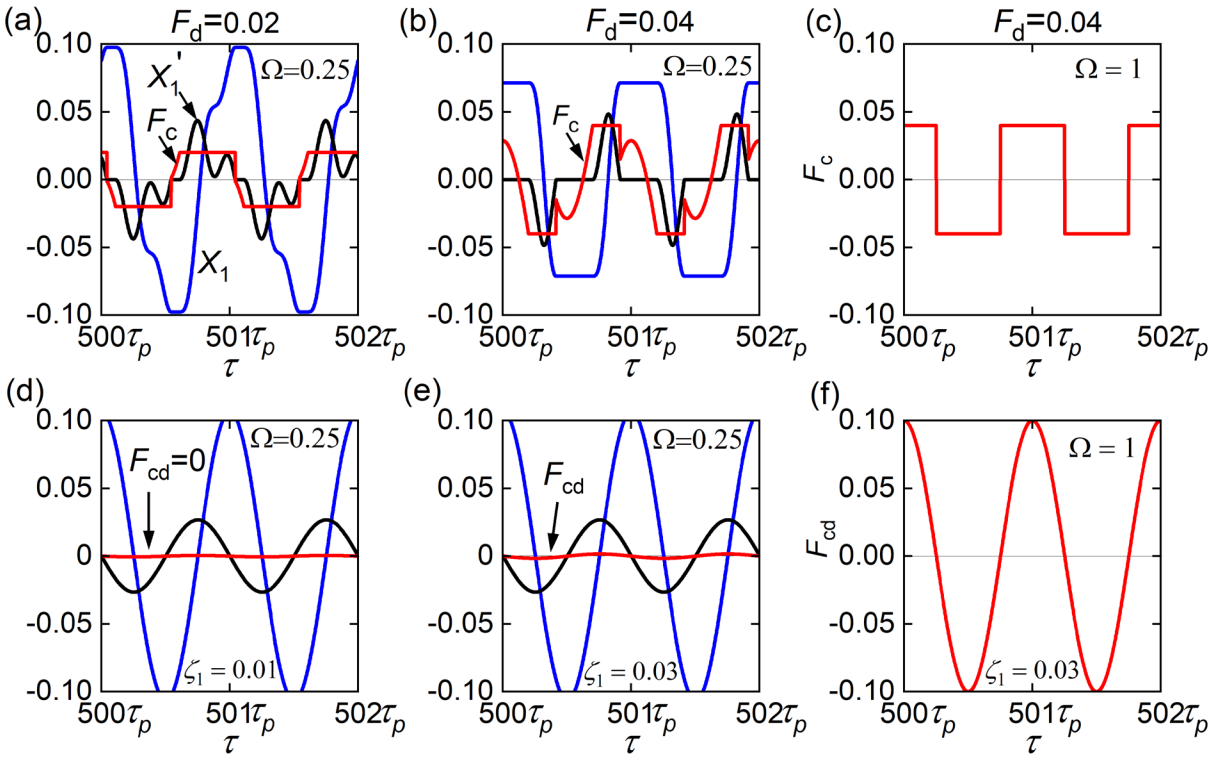

Figure 5. Time histories of the forces and the responses in the steady-state for the system considering dry friction with $F_d = 0.02$ in (a) and $F_d = 0.04$ in (b) and (c), respectively; For the linear system with $\zeta_1 = 0.01$ in (d) and $\zeta_1 = 0.03$ in (e) and (f), respectively. The excitation frequency Ω is Ω = 0.25 in (a), (b), (d) and (e), and Ω = 1 in (c) and (f). The red line is the dry friction force F_c from the frictional contact in (a), (b) and (c), while in (d), (e) and (f) is the damping force F_{cd} from the viscous damper. The blue and black lines are the response displacement and velocity of the mass, respectively.

Figures 5(a) and (b) show the time histories of the displacement responses and the friction force at a low excitation frequency of Ω = 0.25. It shows that the system with dry friction can exhibit stick-slip behaviour in steady-state motion. When increasing the magnitude of friction F_d from 0.02 to 0.04, the displacement response amplitude of the mass is suppressed. In contrast, for the linear system without dry friction in Figs 5(d) and (e), it is found that as the damping ratio ζ_1 of the system damping c_1

increases from 0.01 to 0.03, the viscous damping force is still small and steady-state responses of the mass at the excitation frequency change a little. This behaviour arises from the fact that the viscous damping force F_{cd} is proportional to the velocity. Since the velocity is small at low frequencies, a relatively small damping force is induced by the viscous damper. Figs 5(c) and (f) present the time histories of the friction force and the damping force when the system is excited at $\Omega = 1$ near resonance, respectively. Fig. 5(c) shows that the magnitude of the friction force F_{c} remains as $|F_{\mathrm{c}}| = |F_{\mathrm{d}}| = 0.04$ independent of the excitation frequency. In comparison, Fig. 5(f) shows that there is a significant increase in the amplitude of damping force F_{cd} from the viscous damper at $\Omega = 1$ compared to its amplitude at $\Omega = 0.25$ as shown in Fig. 5(e). This is because that the velocity amplitude near the resonant frequency is relatively large, leading to a larger amplitude of the damping force. Figs 4 and 5 demonstrate that the response amplitude of the mass is sensitive to the changes in the magnitude of friction over a broad frequency range. This is of direct contrast to the influence of viscous damping ratio, which mainly leads to reductions of the peak response.

3.2 Force transmissibility and vibration-energy flow

To evaluate the level of vibration transmission between subsystems of an integrated linear or nonlinear structure, the force transmissibility and time-averaged vibration power flow variables are widely employed as indicators [50]. For the current SDOF system with friction, the force transmissibility TR_{B} can be defined as the ratio between the maximum magnitude of the transmitted force to the base and the amplitude of the excitation force:

$$TR_{\mathrm{B}} = \frac{\max(|\Re\{F_{\mathrm{tB}}\}|)}{F_0}, \tag{23}$$

where F_{tB} represents the non-dimensional transmitted force from mass m_1 to the base. $F_{\mathrm{tB}} = X_1 + 2\zeta_1 X_1'$ is for the system with separated wall and base shown in Fig. 3(a) while $F_{\mathrm{tB}} = F_{\mathrm{c}} + X_1 + 2\zeta_1 X_1'$ is for the system with jointed wall and base shown in Fig. 3(b). For enhanced suppression of vibration transmission, a low value of force transmissibility is desirable.

The instantaneous input power P_{in} and time-averaged input power $\bar{P}_{\mathrm{in}}$ as well as the maximum kinetic energy K_1 of the mass m_1 can be obtained by setting $q = 1$ using Eqs (10), (11) and (12), respectively. The instantaneous dissipated power P_{d1} by the viscous damper c_1 and the instantaneous dissipated power P_{df} by the dry friction contact are expressed as

$$P_{\mathrm{d1}} = 2\zeta_1(\Re\{X_1'\})^2, \qquad P_{\mathrm{df}} = \Re\{X_1'\}\Re\{F_{\mathrm{c}}\}, \tag{24a, 24b}$$

respectively, and the velocity X_1' is obtained by differentiating Eq. (8a) to have $X_1' = \sum_{n=0}^{N} \mathrm{i}n\Omega\tilde{R}_{(1,n)}e^{\mathrm{i}n\Omega\tau}$. The corresponding time-averaged dissipated power are

$$\bar{P}_{\mathrm{d1}} = \frac{1}{\tau_{\mathrm{p}}}\int_{\tau_0}^{\tau_0+\tau_{\mathrm{p}}} P_{\mathrm{d1}}\,\mathrm{d}\tau, \qquad \bar{P}_{\mathrm{df}} = \frac{1}{\tau_{\mathrm{p}}}\int_{\tau_0}^{\tau_0+\tau_{\mathrm{p}}} P_{\mathrm{df}}\,\mathrm{d}\tau\,, \tag{25a, 25b}$$

respectively. The power dissipation ratio provides the proportion of the vibration energy dissipated within the total input energy into the system. The corresponding power dissipation ratios are

$$R_{\mathrm{d1}} = \frac{\bar{P}_{\mathrm{d1}}}{\bar{P}_{\mathrm{in}}}, \qquad R_{\mathrm{df}} = \frac{\bar{P}_{\mathrm{df}}}{\bar{P}_{\mathrm{in}}}, \tag{26a, 26b}$$

for the system viscous damper c_1 and the dry frictional contact, respectively. It is noted that according to the principle of conservation of energy, over a cycle of periodic response, we have $R_{\mathrm{d1}} + R_{\mathrm{df}} = 1$ as all energy input should have been dissipated to have zero net change in the mechanical energy.

In Figs 6, 7 and 8, the influence of frictional contact on the force transmissibility, power flow behaviour and the maximum kinetic energy of the system is presented. The HB-AFT results are represented by different colours of lines while the RK results are denoted by different kinds of symbols. In Fig. 6, the effects of the dry friction on the force transmissibility TR_{B} are illustrated. Fig. 6(a) presents the TR_{B} results for the system with the vertical wall separated from the base, as shown in Fig. 3(a) while Fig. 6(b) shows the TR_{B} results corresponding to the system having a jointed vertical wall and base, as shown in Fig. 3(b). The magnitude of the dry friction F_{d} changes from 0 to 0.02 and to 0.04 in Fig. 6(a) or (b) while the damping ratio ζ_1 of the viscous damper is fixed as $\zeta_1 = 0.01$. The other parameters are set as $V_{\mathrm{d}} = 1 \times 10^{-4}$, $\eta = 1 \times 10^{-4}$ and $F_0 = 0.1$.

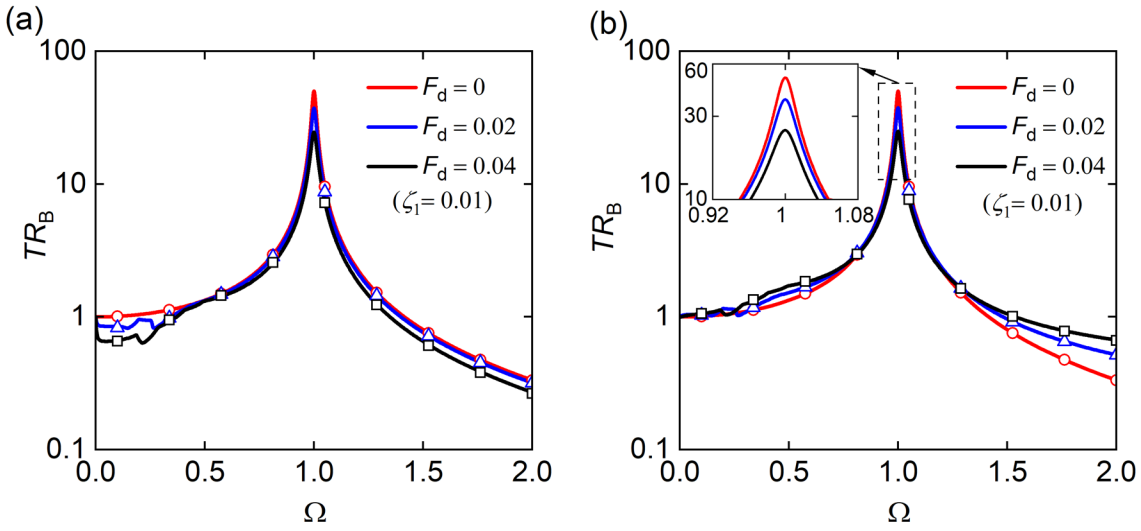

Figures 6(a) and (b) show that variations in the level of dry friction have a relatively large effect on the force transmissibility TR_{B} over a wide frequency band. Fig. 6(a) shows that when the vertical frictional contact wall is separated from the base, as the magnitude of dry friction F_{d} increases from 0 to 0.04, the force transmission to the base is reduced in a broad frequency range due to the frictional resistance. Fig. 6(b) suggests that when the vertical wall is jointed with the base, compared with the reference case for the system without friction (i.e., $F_{\mathrm{d}} = 0$), the increase in the value of F_{d} from 0 to 0.04 leads to reductions in the force transmissibility TR_{B} near the peak frequency $\Omega = 1$. However, at a prescribed frequency in the high-frequency range away from the peak, the force transmissibility increases with F_{d}. This is due to the nonlinearity of the discontinuous friction force introduced into the

system. At the peak frequency, the amplitudes of the displacement and velocity responses are suppressed due to the friction force, resulting in a smaller transmitted force F_{tB} to the base and a smaller value of TR_{B}. At high/low frequencies, the response amplitude is smaller while the amplitude of the friction force is not changed as shown in Fig. 5(b). Therefore, there can be a larger amplitude of F_{tB} and hence a larger value of TR_{B} compared to that of the corresponding linear system ($F_{\mathrm{d}} = 0$).

In Fig. 7, the effects of the dry friction on the time-averaged input power $\bar{P}_{\mathrm{in}}$ into the system and the maximum kinetic energy K_1 of the mass are studied, respectively. Cases 1 and 2 examine the system responses considering the dry friction force F_{d} set as 0.02 and 0.04, respectively, while keeping the damping ratio ζ_1 of the viscous damper constant at 0.01. Cases 3 and 4 are the corresponding linear frictionless systems (i.e., $F_{\mathrm{d}} = 0$) with the damping ratio ζ_1 set as 0.01 and 0.03, respectively. The other system parameters are set as $V_{\mathrm{d}} = 1 \times 10^{-4}$, $\eta = 1 \times 10^{-4}$ and $F_0 = 0.1$. Figure 7(a) shows that the presence of friction for the system in Case 1 results in a relatively lower peak of $\bar{P}_{\mathrm{in}}$, compared with the corresponding system with viscous damping only, i.e., Case 3 with $F_{\mathrm{d}} = 0$. However, at the low or high excitation frequencies, the dry frictional contact leads to a substantial increase in the amount of input power into the oscillating system. The reason for this phenomenon will be further explored in the later content. By a comparison of Cases 1 and 2 with the magnitude of friction F_{d} increasing from 0.02 to 0.04, it is found that the peak value of $\bar{P}_{\mathrm{in}}$ reduces, which is caused by a lower amplitude of resonant velocity due to the stronger frictional resistance. In contrast, when Ω is away from the peak, the increase of F_{d} yields a larger amount of input power into the system. Fig. 7(b) indicates that the presence of the dry friction in Case 1 can lead to a smaller peak value of the maximum kinetic energy K_1, compared to that of frictionless system in Case 3. In the frequency range with the excitation frequency Ω between approximately 0.15 and 0.5, the values of K_1 for Cases 1 and 2 with dry friction become larger than the corresponding values for Cases 3 and 4 without friction. By a comparison of the time histories of the velocity responses of the systems excited at $\Omega = 0.25$, as shown in Figs 5(a) and (d), it is found that the dry friction nonlinearity can yield a larger maximum velocity of the mass, leading to a larger value of kinetic energy. Fig. 7(b) also indicates that in the high-frequency range, the maximum kinetic energy K_1 of the system with dry friction can be smaller than that of the system without friction. Moreover, an increase of the magnitude of friction F_{d} from 0.02 to 0.04 can slightly lower the peak height of K_1 and also reduce the values of K_1 at high excitation frequencies. However, the maximum kinetic energy becomes slightly larger with the increasing F_{d} when Ω locates approximately between 0.25 and 0.5.

In Figs 8(a) and (b), the influence of the magnitude of dry friction on its time-averaged dissipated power $\bar{P}_{\mathrm{df}}$ and the corresponding power dissipation ratio R_{df} is investigated. Three cases are considered by changing the value of F_{d} from 0.01 to 0.02 and to 0.04. The other parameters are set as $\zeta_1 = 0.01$, $V_{\mathrm{d}} = 1 \times 10^{-4}$, $\eta = 1 \times 10^{-4}$ and $F_0 = 0.1$. Figure 8(a) shows that as the magnitude of friction F_{d} increases from 0.01 to 0.04, there is more power dissipation by the dry friction contact in a wide frequency band. Fig. 8(b) shows that there is a minimum value of the power dissipation ratio R_{df}

associated with dry friction at the resonant frequency of $\Omega = 1$. As the excitation frequency increases from 0 to 2, the value of R_{df} firstly decreases from approximately 1 to a local minimum, and then increases to the value close to 1. It suggests that the frictional contact is effective for energy dissipation when the system is not in resonance. By increasing the magnitude of friction from 0.01 to 0.04, the value of the local minimum point of R_{df} increases substantially. In comparison, when the excitation frequency is away from $\Omega = 1$, the changes in F_{d} lead to much smaller variations in R_{df}.

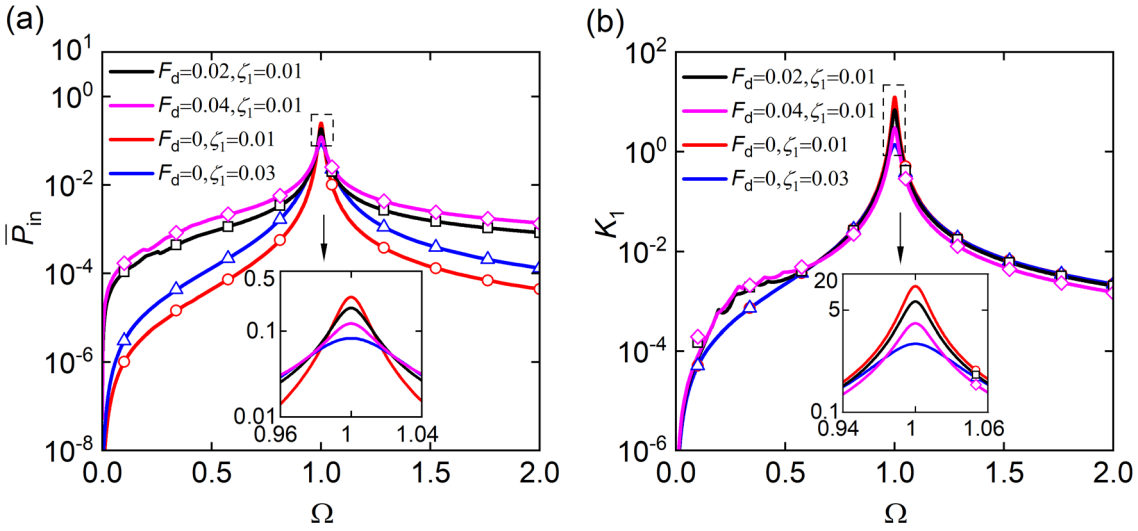

Figure 7. Effects of the magnitude of friction F_{d} on (a) the time-averaged input power $\bar{P}_{\mathrm{in}}$ into the system and (b) the maximum kinetic energy K_1 of the mass. The black and pink lines are for the nonlinear system having dry friction with $F_{\mathrm{d}} = 0.02$ and 0.04, respectively. The red and blue lines are for the linear system with $\zeta_1 = 0.01$ and 0.03, respectively. Square, diamond, circular and triangular symbols denote RK results.

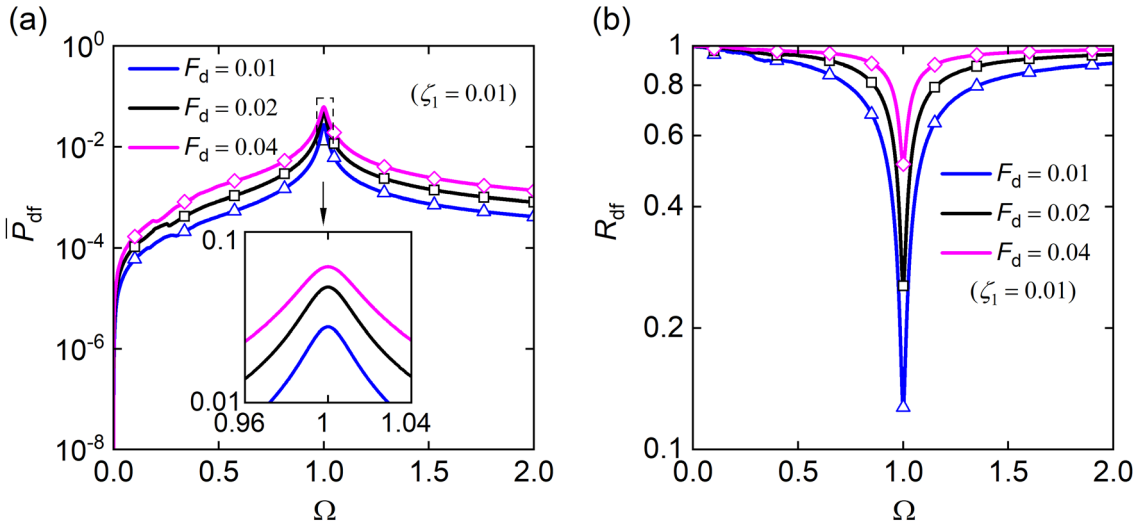

Figure 8. Effects of the magnitude of friction F_{d} on (a) the time-averaged dissipated power by the dry friction contact $\bar{P}_{\mathrm{df}}$ and (b) the corresponding power dissipation ratio R_{df}. The system parameters are fixed as $\zeta_1 = 0.01$, $V_{\mathrm{d}} = 1 \times 10^{-4}$, $\eta = 1 \times 10^{-4}$ and $F_0 = 0.1$. The blue, black and pink lines are for the nonlinear system having dry friction with $F_{\mathrm{d}} = 0.01$, 0.02 and 0.04, respectively. Triangular, square and diamond symbols denote RK results.

In Fig. 9, the mechanisms for the friction influence on $\bar{P}_{\mathrm{in}}$ and $\bar{P}_{\mathrm{df}}$ at low frequencies shown in Figs 7(a) and 8(a), are further explored. Figs 9(a) and (b) present the time histories of the steady-state instantaneous input power P_{in} into the system with the magnitude of friction $F_{\mathrm{d}} = 0.02$ and 0.04,

respectively, while setting damping ratio $\zeta_1 = 0.01$. For comparison, Figs 9(d) and (e) present the P_{in} for the corresponding linear frictionless systems with the damping ratio ζ_1 being 0.01 and 0.03, respectively. The excitation frequency is prescribed to be $\Omega = 0.25$ and the other system parameters are set the same as those used in Figs 6, 7 and 8. Figs 9(a) and (b) show the stick-slip characteristic at low frequencies for the system with dry friction, making the positive part of the instantaneous input power to be significantly larger than the negative part. When increasing the magnitude of friction F_{d} from 0.02 to 0.04, the negative part of P_{in} is further reduced while the positive part is increased, leading to a much larger amount of input energy into the system over one cycle of periodic response. Compared to the P_{in} in the linear frictionless systems shown in Figs 9(d) and (e), it is found that the increase of damping ratio ζ_1 from 0.01 to 0.03 has a smaller effect on the P_{in} at this frequency. Fig. 9(c) depicts the time histories of the instantaneous dissipated power P_{df} by the friction at $\Omega = 0.25$ with $F_{\text{d}} = 0.02$ or $F_{\text{d}} = 0.04$. It shows that in the low-frequency range, the increase in the magnitude of friction can lead to a much larger amount of power dissipation by the frictional contact. In comparison, Fig. 9(f) presents the time histories of the instantaneous dissipated power P_{d1} by the viscous damper c_1 of the corresponding linear system at the same frequency of $\Omega = 0.25$. It shows that the increase of the damping ratio ζ_1 from 0.01 to 0.03 has little influence on the power dissipation P_{d1} when the excitation frequency is low. From Figs 7, 8 and 9, it can be deduced that comparing to viscous damping, the dry friction nonlinearity can strongly affect the energy flow characteristics of the system when the excitation frequency is away from the resonance.

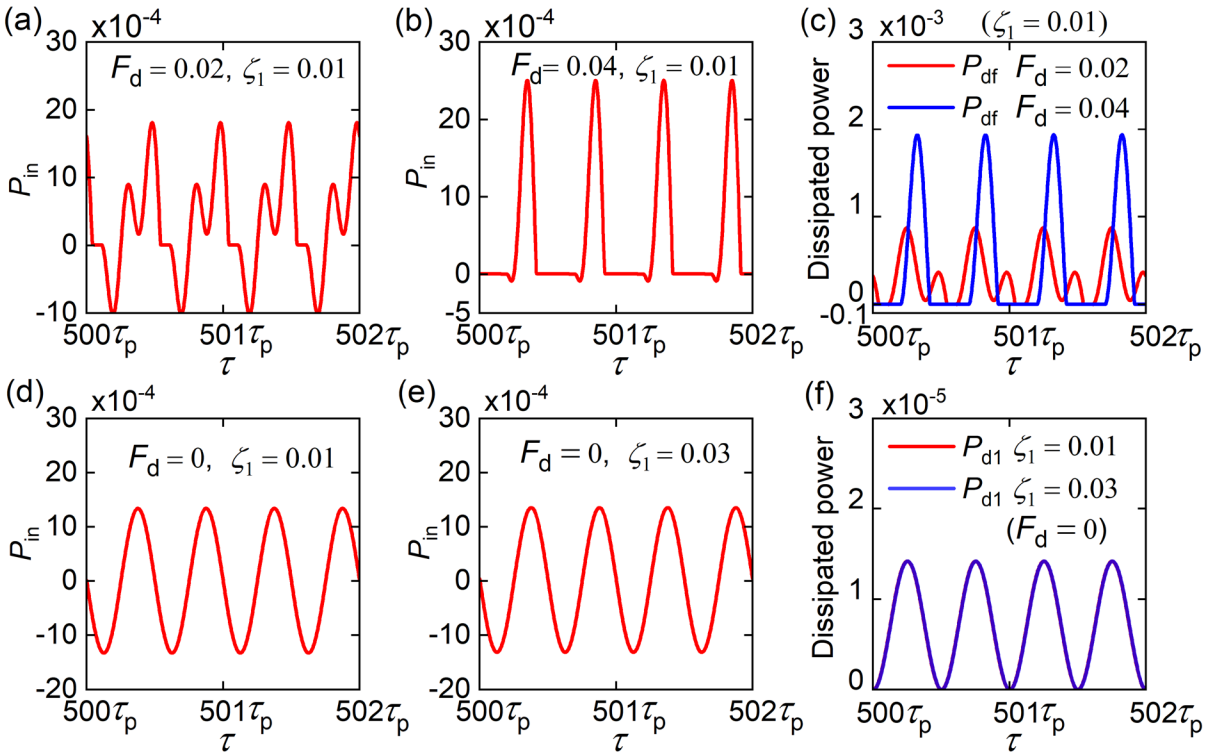

Figure 9. Time histories of instantaneous power flow in the steady state at $\Omega = 0.25$ for the system with dry friction in (a), (b) and (c), and for the frictionless linear system in (d), (e) and (f). In (a), (b), (d) and (e): the instantaneous input power P_{in}; in (c): the instantaneous power dissipation P_{df} by the dry friction contact, and the red and blue lines are for the frictional system with $F_{\text{d}} = 0.02$ and 0.04, respectively; in (f): the instantaneous

power dissipation P_{d1} by the system viscous damper, and the red and blue lines are for the frictionless system with $\zeta_1 = 0.01$ and 0.03, respectively.

4 Energy flow of 2DOF system coupled with frictional contact

In this section, the vibration transmission and energy dissipation characteristics of a coupled system with dry friction at the interface are investigated. The mathematical model of the 2DOF system with interfacial friction is firstly introduced. Then, the approaches for determining the dynamic response of the system by the HB-AFT or numerical integration methods are discussed. The force transmissibility and vibration energy flow for the coupled system are subsequently formulated. Finally, the dynamics and vibration energy flow results of the coupled system are presented. In particular, the effects of the interfacial friction on the vibration transmission and energy dissipation within the system are examined.

4.1 Mathematical modelling

Figure 10(a) shows two SDOF systems, each representing a dominant mode of a substructure, connected via a spring of stiffness coefficient k_3. The SDOF primary system comprises the primary mass m_1 subjected to a harmonic force excitation with amplitude of f_0 and frequency of ω, a linear spring with a stiffness coefficient k_1 and a viscous damper with damping c_1. The SDOF secondary system has the secondary mass m_2, a viscous damper of damping c_2, and a linear spring with stiffness k_2. The primary mass is sliding on the rough surface of the secondary mass, where the interactive dry friction force f_c is generated between two masses with the magnitude of friction f_d. The secondary system is placed horizontally on the smooth surface. The static equilibrium positions of the two masses, where $x_1 = x_2 = 0$ and the springs k_1, k_2, k_3 are undeformed, are set as the reference. To highlight the influence of dry friction on the energy flow and vibration transmission, the frictional contact can be replaced by a viscous damper at the interface with damping coefficient c_d for comparison.

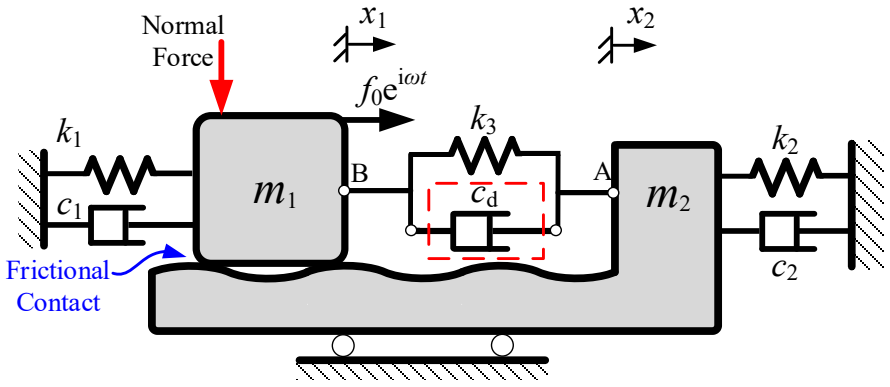

Figure 10. A 2DOF system with SDOF sub-systems coupled by a linear spring k_3 and the nonlinear dry frictional contact or a viscous damper c_d at the interface. The primary SDOF system with mass of m_1 is excited by a harmonic force $f_0e^{i\omega t}$ and the secondary SDOF system with mass of m_2 is placed on a horizontal smooth surface.

The equations of motion of the system can be written in a matrix form as

$$\begin{bmatrix} m_1 & 0 \\ 0 & m_2 \end{bmatrix}\begin{Bmatrix} \ddot{x}_1 \\ \ddot{x}_2 \end{Bmatrix} + \begin{bmatrix} c_1 & 0 \\ 0 & c_2 \end{bmatrix}\begin{Bmatrix} \dot{x}_1 \\ \dot{x}_2 \end{Bmatrix} + \begin{bmatrix} k_1 + k_3 & -k_3 \\ -k_3 & k_2 + k_3 \end{bmatrix}\begin{Bmatrix} x_1 \\ x_2 \end{Bmatrix} + \begin{Bmatrix} f_c \\ -f_c \end{Bmatrix} = \begin{Bmatrix} f_0 e^{i\omega t} \\ 0 \end{Bmatrix}, \quad (27)$$

where f_c represents the dry friction force at the interface being a function of the relative velocity $v_r = \dot{x}_1 - \dot{x}_2$. The friction can be determined by using the Karnopp model and the tanh-regularization approach expressed in Eqs (3) and (4), respectively. When the Karnopp model, as shown in Eq. (3), is used, considering the stick state with no relative motion between the masses, i.e., $\dot{x}_1 = \dot{x}_2$ and $\ddot{x}_1 = \ddot{x}_2$. The resultant external force f_e applied to the coupling interface in the tangential direction is balanced by the friction force f_c. From Eq. (27), we have

$$f_e = f_c = k_3(x_2 - x_1) + \frac{1}{m_1+m_2}[m_1k_2x_2 + (m_1c_2 - m_2c_1)\dot{x}_1 + m_2f_0e^{i\omega t} - m_2k_1x_1]. \quad (28)$$

Here the new parameters are defined as

$$\omega_2 = \sqrt{\frac{k_2}{m_2}}, \quad \zeta_2 = \frac{c_2}{2m_2\omega_2}, \quad X_2 = \frac{x_2}{l_0}, \quad \gamma = \frac{\omega_2}{\omega_1}, \quad \rho = \frac{c_d}{c_1}, \quad \mu = \frac{m_2}{m_1}, \quad \kappa = \frac{k_3}{k_1}, \quad (29a\text{-}29g)$$

where ω_2 and ζ_2 are the undamped natural frequency and the damping ratio for the secondary system without friction, respectively, X_2 denotes the non-dimensional displacement of the secondary mass, γ is the ratio between the undamped natural frequency of the primary system and that of the secondary system, ρ represents the damping level of the interfacial viscous damper which is used to replace the dry friction contact for comparison purpose, μ is the mass ratio and κ is the stiffness ratio for the linear spring at the interface. By using them and previously defined parameters in Eq. (14), Eq. (27) can be transformed into a dimensionless form as

$$\begin{bmatrix}1 & 0\\ 0 & \mu\end{bmatrix}\begin{bmatrix}X_1''\\ X_2''\end{bmatrix} + \begin{bmatrix}2\zeta_1 & 0\\ 0 & 2\mu\zeta_2\gamma\end{bmatrix}\begin{bmatrix}X_1'\\ X_2'\end{bmatrix} + \begin{bmatrix}1+\kappa & -\kappa\\ -\kappa & \mu\gamma^2+\kappa\end{bmatrix}\begin{bmatrix}X_1\\ X_2\end{bmatrix} + \begin{Bmatrix}F_c\\ -F_c\end{Bmatrix} = \begin{Bmatrix}F_0e^{i\Omega\tau}\\ 0\end{Bmatrix}, \quad (30)$$

where F_c is the non-dimensional dry friction force which can be expressed by replacing X_1' with $(X_1' - X_2')$ in Eq. (21) and Eq. (22) for the use of the tanh-regularization approach and the Karnopp model, respectively. In Eq. (22) when using the Karnopp model, F_e is the dimensionless resultant external force applied to the coupling interface in the tangential direction from Eq. (28):

$$F_e = \frac{f_e}{k_1l_0} = \kappa(X_2 - X_1) + \frac{\mu}{1+\mu}[\gamma^2X_2 + 2(\zeta_2\gamma - \zeta_1)X_1' + F_0e^{i\Omega\tau} - X_1]. \quad (31)$$

For the corresponding case of using an interfacial viscous damper to replace the dry friction contact, the friction force term F_c in Eq. (30) is replaced with the damping force term $F_{cd} = 2\zeta_1\rho(X_1' - X_2')$ by the interfacial viscous damper.

To obtain the steady-state response of the coupled system, Eq. (30) can be solved using a combined use of the HB-AFT method and numerical continuations illustrated in Subsection 2.2, where the tanh-regularization approach is used for the approximation of the friction force. The results are compared with the Runge-Kutta method with the friction force determined by the Karnopp model.

4.2 Force transmissibility and vibration-energy flow

The influence of the interfacial frictional contact on the vibration transmission between the two subsystems and the vibration energy dissipation at the interface is of interest. The force transmissibility from the primary mass m_1 to the secondary mass m_2 is expressed by

$$TR_{\mathrm{S}} = \frac{\max(\Re\{|F_{\mathrm{ts}}|\})}{F_0}, \tag{32}$$

where $F_{\mathrm{ts}} = \kappa(X_1 - X_2) + F_{\mathrm{c}}$ is the dimensionless transmitted force to mass m_2 for the systems with dry friction. It is noted that when viscous damping, instead of dry friction, exists at the interface, the transmitted force is replaced with $F_{\mathrm{ts}} = \kappa(X_1 - X_2) + F_{\mathrm{cd}}$.

For the current system in the steady-state motion, the non-dimensional time-averaged input power $\bar{P}_{\mathrm{in}}$ over one cycle of periodic response is obtained from Eq. (11) by setting $q = 1$. The time-averaged dissipated power $\bar{P}_{\mathrm{d1}}$ by the viscous damper c_1 is still defined by Eq. 25(a). Over one cycle of periodic motion, the time-averaged transmitted power to the secondary system is entirely dissipated by the damper c_2. Therefore, the time-averaged transmitted power P_{ts} to the secondary system and the time-averaged dissipated power $\bar{P}_{\mathrm{di}}$ by the interfacial dissipative element in the form of a friction contact or a viscous damper, are expressed as

$$\bar{P}_{\mathrm{ts}} = \frac{1}{\tau_{\mathrm{p}}}\int_{\tau_0}^{\tau_0+\tau_{\mathrm{p}}} P_{\mathrm{ts}}\,\mathrm{d}\tau, \qquad \bar{P}_{\mathrm{di}} = \frac{1}{\tau_{\mathrm{p}}}\int_{\tau_0}^{\tau_0+\tau_{\mathrm{p}}} P_{\mathrm{di}}\,\mathrm{d}\tau, \tag{33a, 33b}$$

respectively. The corresponding instantaneous transmitted power P_{ts} and the instantaneous dissipated power P_{di} are

$$P_{\mathrm{ts}} = 2\mu\zeta_2\gamma(\Re\{X_2'\})^2, \tag{34a}$$

$$P_{\mathrm{di}} = \begin{cases} \Re\{X_1' - X_2'\}\Re\{F_{\mathrm{c}}\}, & \text{for the dry frictional contact,} \\ 2\zeta_1\rho\,(\Re\{X_1' - X_2'\})^2, & \text{for the interfacial viscous damper,} \end{cases} \tag{34b}$$

respectively. X_1' and X_2' are obtained by taking the differentiation of X_1 and X_2 as $X_1' = \sum_{n=0}^{N} in\Omega\tilde{R}_{(1,n)}\mathrm{e}^{in\Omega\tau}$ and $X_2' = \sum_{n=0}^{N} in\Omega\tilde{R}_{(2,n)}\mathrm{e}^{in\Omega\tau}$, respectively. The power dissipation ratio R_{d1} by the damper c_1 is still obtained from Eq. (26a). The power dissipation ratio R_{di} at the interface and the power transmission ratio R_{ts} are defined as

$$R_{\mathrm{di}} = \frac{\bar{P}_{\mathrm{di}}}{\bar{P}_{\mathrm{in}}}, \qquad R_{\mathrm{ts}} = \frac{\bar{P}_{\mathrm{ts}}}{\bar{P}_{\mathrm{in}}}, \tag{35a, 35b}$$

respectively. It is noted that in accordance with the principle of conservation of energy, over a period of cyclic response, we have $R_{\mathrm{di}} + R_{\mathrm{ts}} + R_{\mathrm{d1}} = 1$.

4.3 Dynamics and vibration-energy flow results

Here case studies are performed to investigate the influence of friction at the coupling interface on the vibration transmission through the interface and dissipation in the coupled system. Both HB approximations and numerical integration results are obtained and presented. Case 1 corresponds to the linear system with only a spring at the interface ($F_{\mathrm{d}} = \rho = 0$). Case 2 and 3 consider the presence of dry friction at the interface with different magnitude of dry friction. The damping ratio in these two cases is fixed as $\rho = 0$. To highlight the influence of dry friction on vibration transmission and energy flow, Case 4 presents the frictionless system having an interfacial viscous damper with the damping ratio $\rho = 4$. For all four cases, the system parameters are set as $\zeta_1 = \zeta_2 = 0.01, \gamma = 1, \mu = 1, \kappa = 1, V_{\mathrm{d}} = 1 \times 10^{-4}, \eta = 1 \times 10^{-4}$ and $F_0 = 0.5$. Different colours of lines represent the results of the

HB-AFT approximation based on the tanh-regularization approach. Different types of symbols are used to denote the results by using the Runge-Kutta method based on the Karnopp friction model.

In Figs 11(a) and (b), the effects of the interfacial friction on the steady-state maximum displacement responses $X_{1\_\max}$ and $X_{2\_\max}$ of the primary and the secondary masses are presented. Two peaks are observed in each curve of $X_{1\_\max}$ and $X_{2\_\max}$. An anti-peak is found in each curve of $X_{1\_\max}$ shown in Fig. 11(a). By conducting modal analysis on the corresponding linear system without friction ($F_{\mathrm{d}} = \rho = 0$), it is found that the first peak is corresponding to the in-phase mode while the second corresponds to the out-of-phase mode. Fig. 11(a) shows that compared to the linear system in Case 1 with only a spring at the interface (i.e., $F_{\mathrm{d}} = \rho = 0$), the interfacial friction with $F_{\mathrm{d}} = 0.10$ or 0.15 in Cases 2 or 3 leads to minor changes in the first peak of $X_{1\_\max}$ near $\Omega = 1$ but a substantial reduction in its second peak value. This is because at the first peak frequency, two masses have in-phase motion and the relative velocity between the two masses is small, therefore, the dry frictional contact has a small effect on the motion of two masses. However, at the second peak frequency near $\Omega = 1.74$ corresponding to the out-of-phase mode, the masses are moving in opposite directions such that the friction acts as a resistance force for the motion of both masses. As a result, the displacement responses of two masses are suppressed by the friction force. Fig. 11(a) also shows that compared with Case 4 considering an interfacial viscous damper with $\rho = 4$, the interfacial friction in Cases 2 and 3 results in smaller values of $X_{1\_\max}$ at low or high excitation frequencies, but larger values of $X_{1\_\max}$ when Ω is near the second peak or the anti-peak. Moreover, as the magnitude of friction F_{d} increases from 0.10 to 0.15, there is an increase in the anti-peak value of $X_{1\_\max}$ but further reductions in the second peak value as well as the values in the low- or high-frequency ranges. Fig. 11(b) shows that compared to Case 1 with $F_{\mathrm{d}} = \rho = 0$, the existence of the interfacial friction can substantially reduce the second peak value of $X_{2\_\max}$ but its first peak value is less affected. This is again due to the differences in the dominant modes. At a prescribed excitation frequency Ω away from the peaks, the interfacial viscous damping with $\rho = 4$ considered in Case 4 yields similar values of $X_{2\_\max}$ compared to that in the reference Case 1. In contrast, the interfacial friction in Cases 2 and 3 leads to a significant increase in the values of $X_{2\_\max}$ compared with Case 1, particularly at high frequencies. With the increase of Ω, the differences in the values of $X_{2\_\max}$ between the viscous damper case (i.e., Case 4) and frictional contact cases (i.e., Cases 2 and 3) become larger. Fig. 11(b) also shows that when F_{d} changes from 0.10 to 0.15, the height of the second peak of $X_{2\_\max}$ is further reduced due to a larger interfacial friction force resisting the vibration. However, the values of $X_{2\_\max}$ increase at low or high frequencies. This behaviour is further explored in Fig. 12.

Figures 12(a), (b), (d) and (e) present the steady-state time histories of the friction force and the velocities of the system with interfacial dry friction excited at $\Omega = 0.4$, $\Omega = 1.41$, $\Omega = 1.74$ and $\Omega = 3$, respectively. The magnitude of friction is set as $F_{\mathrm{d}} = 0.15$ while $\rho = 0$. For comparison, Figs 12(c) and (f) show the time histories of the velocity responses and the interfacial viscous damping force of

the frictionless system with $\rho = 4$ and $F_d = 0$ excited at $\Omega = 1.41$ and $\Omega = 3$, respectively. The other parameters are the same as those used in Fig. 11. The red lines in Figs 12(a), (b), (d) and (e) represent the interfacial friction force F_c, while those in Figs 12(c) and (f) denote the interfacial damping force F_{cd}. The blue and black lines correspond to the velocities X_1' and X_2' of two masses, respectively.

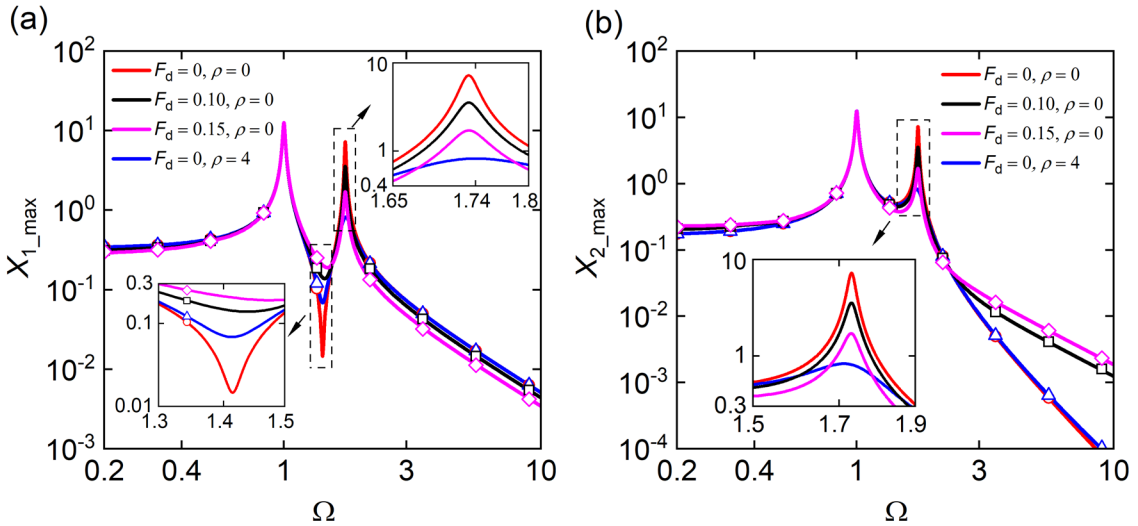

Figure 11. Effects of the magnitude of friction F_d on the steady-state maximum response displacement (a) X_{1_max} for the primary mass and (b) X_{2_max} for the secondary mass, respectively. The red and blue lines are for the linear system with $\rho = 0$ and 4, respectively. The black and pink lines are for the nonlinear system having dry friction at the interface with $F_d = 0.10$ and 0.15, respectively. Symbols: RK results.

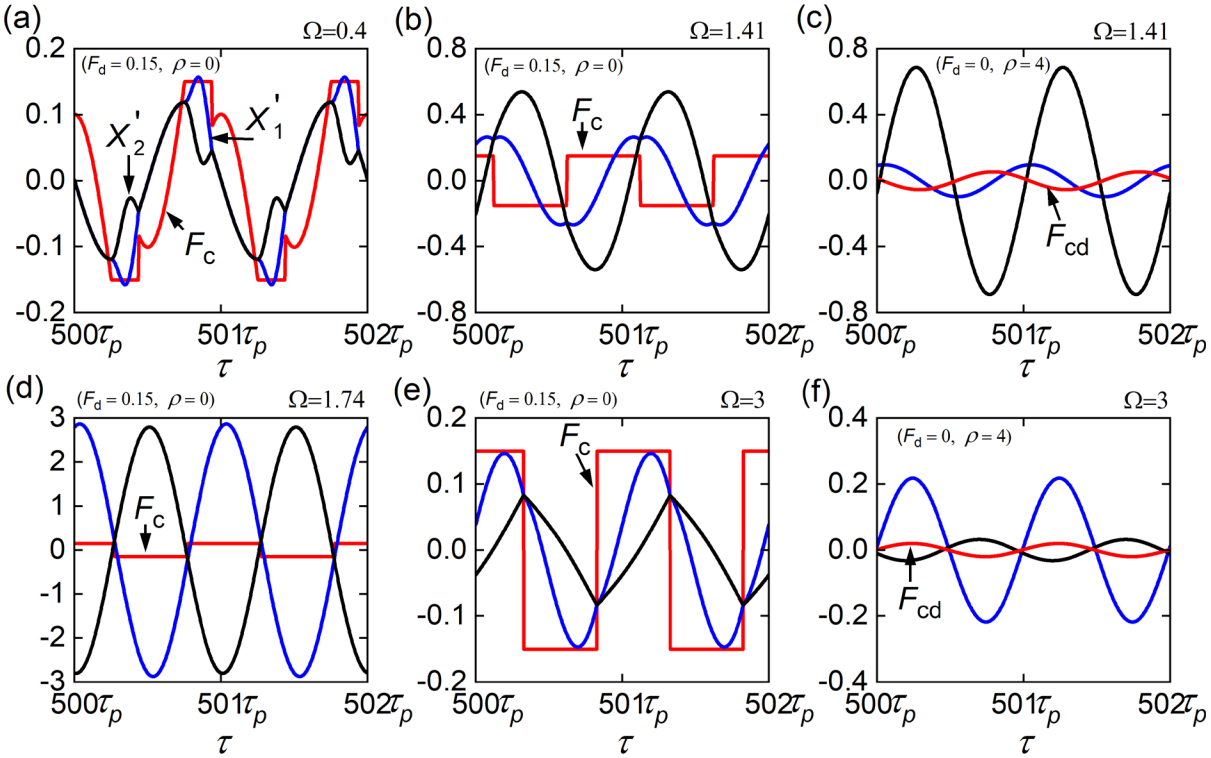

Figure 12. Time histories of the forces and the velocity responses in steady-state for the frictional contact case with $F_d = 0.15$, $\rho = 0$ at (a) $\Omega = 0.4$, (b) $\Omega = 1.41$, (d) $\Omega = 1.74$ and (e) $\Omega = 3$, respectively; For the viscous damper case with $F_d = 0$, $\rho = 4$ at (c) $\Omega = 1.41$ and (f) $\Omega = 3$, respectively. The red line is the dry friction force F_c by the interfacial friction contact in (a), (b), (d) and (e), while in (c) and (f) is the damping force F_{cd} by the interfacial viscous damper. The blue and black lines are the response velocity of the primary and the secondary masses, respectively.

Figure 12(a) shows that at a low excitation frequency of $\Omega = 0.4$, over a portion of an excitation cycle, the two masses are in the stick state and moving at the same velocity, i.e., $X_1' = X_2'$. By examining the time history of the friction force F_c in Fig. 12(a), it is known that the magnitude of the resultant external force F_e has not reached the maximum static friction force, i.e., the magnitude of friction F_d. However, when the absolute value of X_1' becomes larger than a certain value, the stick state at the interface is switched into the slip state because F_e becomes larger than F_d. In the slip region, the value of the friction force remains as a constant, i.e., $F_c = F_d$. As $|X_1'| > |X_2'|$ in the slip state, the friction force acts in the same direction as the moving direction of mass m_2 but opposite to the motion of mass m_1. Consequently, the interfacial friction can lead to a larger maximum displacement of the secondary mass but a smaller maximum displacement of the primary mass at low excitation frequencies, as shown in Fig. 11. Fig. 12(b) demonstrates that for the system with dry friction excited near the frequency of the anti-peak in the frequency response shown in Fig. 11(a), there exists a phase difference of approximately $\pi/2$ between the periodic velocity responses of two masses.

By comparing to the velocity responses in the corresponding system with interfacial viscous damping at the same excitation frequency shown in Fig. 12(c), it is found that the dry friction at the coupling interface can lead to a much higher amplitude of X_1' but a lower amplitude of X_2'. Fig. 12(d) shows that when the excitation frequency Ω is $\Omega = 1.74$ at the second peak in the frequency response curves shown in Fig. 11, two masses are moving in opposite directions and the motions are hence suppressed by the frictional resistance force at the interface. By comparing the time histories of the velocities with interfacial dry friction or viscous damping at high frequencies away from peaks, e.g., $\Omega = 3$, as shown by Figs 12(e) and (f), it is found that the amplitude of the friction force by the frictional contact can be much larger than that of the damping force by the interfacial viscous damper at this frequency. The frictional contact case has a smaller amplitude of the response velocity X_1' but a larger amplitude of X_2'.

In Fig. 13, the influence of the magnitude of the interfacial friction on the steady-state maximum relative displacement $|X_1 - X_2|_{max}$ between two masses is studied. Only one peak can be found in each curve of $|X_1 - X_2|_{max}$ at the out-of-phase mode of the corresponding linear system. It shows that compared to Case 1 with $F_d = \rho = 0$, the presence of the dry friction at the interface in Cases 2 and 3 (with $F_d = 0.10$ and 0.15, respectively) can reduce the values of $|X_1 - X_2|_{max}$ in a wide frequency band. The reason is that the dry friction force at the interface always resista motions of the two masses when moving in oposite directions. As a result, the existence of the frictional contact at the interface can suppress the relative motion of the coupled masses in a broad frequency range. Fig. 13 also shows that compared to Case 4 having an interfacial viscous damper with $\rho = 4$, Cases 2 and 3 with dry friction at the interface have a higher peak of $|X_1 - X_2|_{max}$ but much lower values of $|X_1 - X_2|_{max}$ at low or high frequencies. At a prescribed excitation frequency, as the magnitude of friction F_d increases from 0.10 to 0.15, there is a further reduction in the value of $|X_1 - X_2|_{max}$ due to a stronger frictional

resistance force. It can be summarized that the interfacial friction can effectively attenuate the amplitude of the relative motion between the coupled masses when Ω locates in the low- or high-frequency ranges.

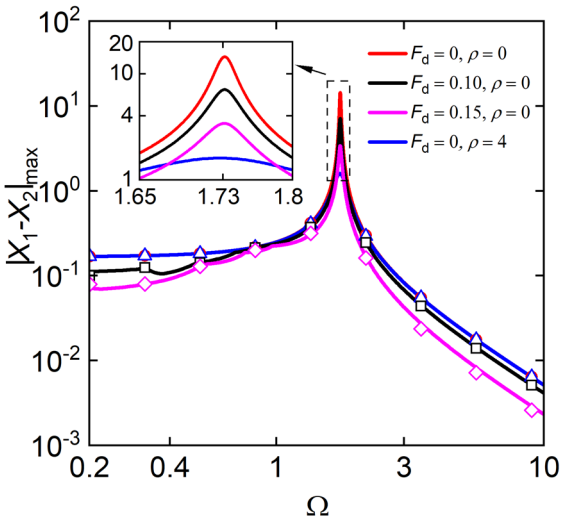

Figure 13. Effects of the magnitude of friction F_d on the steady-state maximum relative displacement $|X_1 - X_2|_{max}$ between two masses. The red and blue lines are for the linear system with $\rho = 0$ and 4, respectively. The black and pink lines are for the nonlinear system having dry friction at the interface with $F_d = 0.10$ and 0.15, respectively. Symbols: RK results.

In Figs 14(a) and (b), the effects of the interfacial friction on the force transmissibility TR_S to the secondary mass and the time-averaged input power $\bar{P}_{in}$ into the system are investigated, respectively. Only one peak is observed in each curve of TR_S in Fig. 14(a), which is corresponding to the out-of-phase mode of the linear system with $F_d = \rho = 0$. In Fig. 14(b), two peaks can be found in each curve of $\bar{P}_{in}$. Fig. 14(a) shows that compared to the reference linear system considered in Case 1 with $F_d = \rho = 0$, the presence of the interfacial friction in Cases 2 and 3 (with $F_d = 0.05$ and 0.15, respectively) can lead to a slight reduction in the peak value of TR_S but significantly larger values of TR_S when the excitation frequency is away from the peak. The reason is that at the peak frequency ($\Omega \approx 1.74$), the masses are moving in the opposite directions, the friction force acting at the coupling interface restrains the relative motion of two masses. Therefore, a smaller spring force at the interface is obtained due to the smaller relative displacement between masses, resulting in a smaller total transmitted force and a lower peak of TR_S.

At low or high excitation frequencies, the relative displacement between the masses is small, leading to a relatively small spring force at the coupling interface. Based on the Karnopp friction model expressed in Eq. (22), the amplitude of friction force is only depending on the magnitude relationship between the resultant external forces applied at the interface, F_e and F_d. In the low- or high-frequency ranges, the amplitude of friction force is a constant as the same to the magnitude of friction F_d. Therefore, the existence of the interfacial dry friction can increase the maximum total transmitted force to the mass m_2 via the interface in those frequency ranges and results in larger force transmissibility TR_S. Moreover, Fig. 14(a) shows that as the excitation frequency further increases, the value of TR_S in Cases 2 and 3 with dry friction may become close to a constant value. This is because with the increasing

frequency, the force generated by the interfacial spring becomes smaller and the value of the maximum magnitude of the transmitted force in Eq. (32) becomes approximately equal to the constant value of the magnitude of friction F_d. Fig. 14(a) also shows that an increase of F_d from 0.05 to 0.15 can further reduce the peak value of TR_S but increase the values of TR_S when the excitation frequency Ω is away from the resonance. Fig. 14(b) shows that the presence of dry friction has negligible effect on the first peak of time-averaged input power at $\Omega = 1$ but can suppress the second peak of $\bar{P}_{in}$ near $\Omega = 1.74$. The figure also shows that compared with Case 1, the existence of interfacial friction in Cases 2 or 3 or viscous damping in Case 4 can increase the amount of input power into the system in the low- or high-frequency ranges. However, the cases with interfacial friction can have much larger values of $\bar{P}_{in}$ when Ω is away from the peak frequencies. When increasing the magnitude of friction from 0.05 to 0.15, the second peak value of $\bar{P}_{in}$ is further reduced but the value of $\bar{P}_{in}$ increases at a prescribed value of Ω away from the peaks.

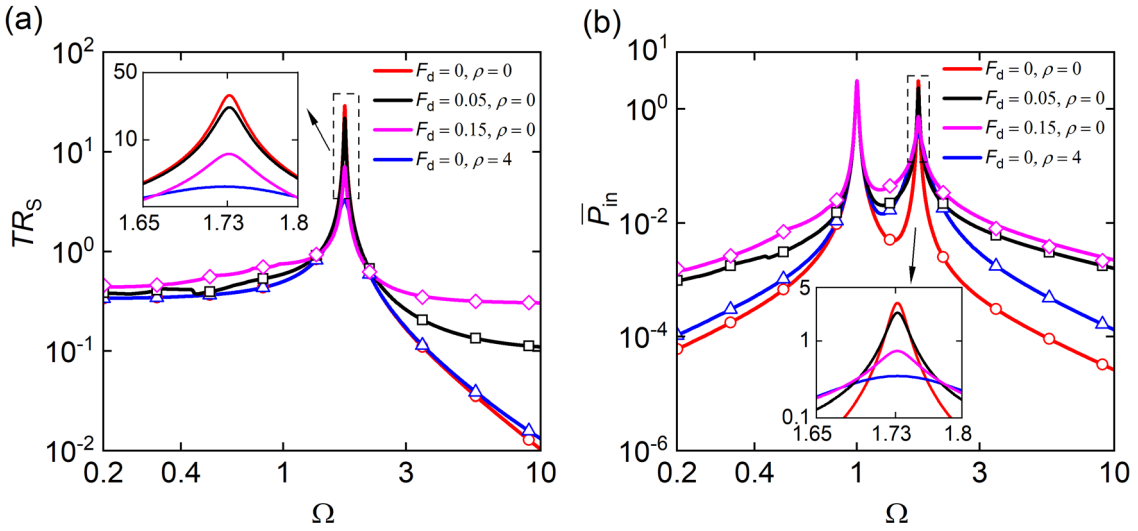

Figure 14. Effects of the magnitude of friction F_d on (a) the force transmissibility to the secondary system TR_S and (b) the time-averaged input power $\bar{P}_{in}$ into the system, respectively. The red and blue lines are for the linear system with $\rho = 0$ and 4, respectively. The black and pink lines are for the nonlinear system having dry friction at the interface with $F_d = 0.05$ and 0.15, respectively. Circular, square, diamond and triangular symbols denote RK results.

In Figs 15(a) and (b), the influence of the interfacial friction on the time-averaged transmitted power $\bar{P}_{ts}$ to the secondary system and the power transmission ratio R_{ts} is examined, respectively. In Fig. 15(a), two peaks can be found in each curve of $\bar{P}_{ts}$, of contrast to the force transmissibility TR_S curve in Fig. 14(a), where only one peak is observed in each curve. This phenomenon indicates that attention would be placed on the proper use of performance indices for the evaluation of the vibration transmission level. Figure 15(a) shows that compared with the reference linear system in Case 1 with $F_d = \rho = 0$, it is found that the interfacial friction with $F_d = 0.05$ or 0.15 in Cases 2 or 3 can reduce the amount of power transmitted to the secondary system near the second peak frequency at $\Omega \approx 1.74$. When comparing the power transmission between Case 4 considering the interfacial viscous damping

with $\rho = 4$ and that of the dry friction cases, the presence of dry friction can significantly increase the amount of power transmission to the secondary system, especially in the high-frequency range.

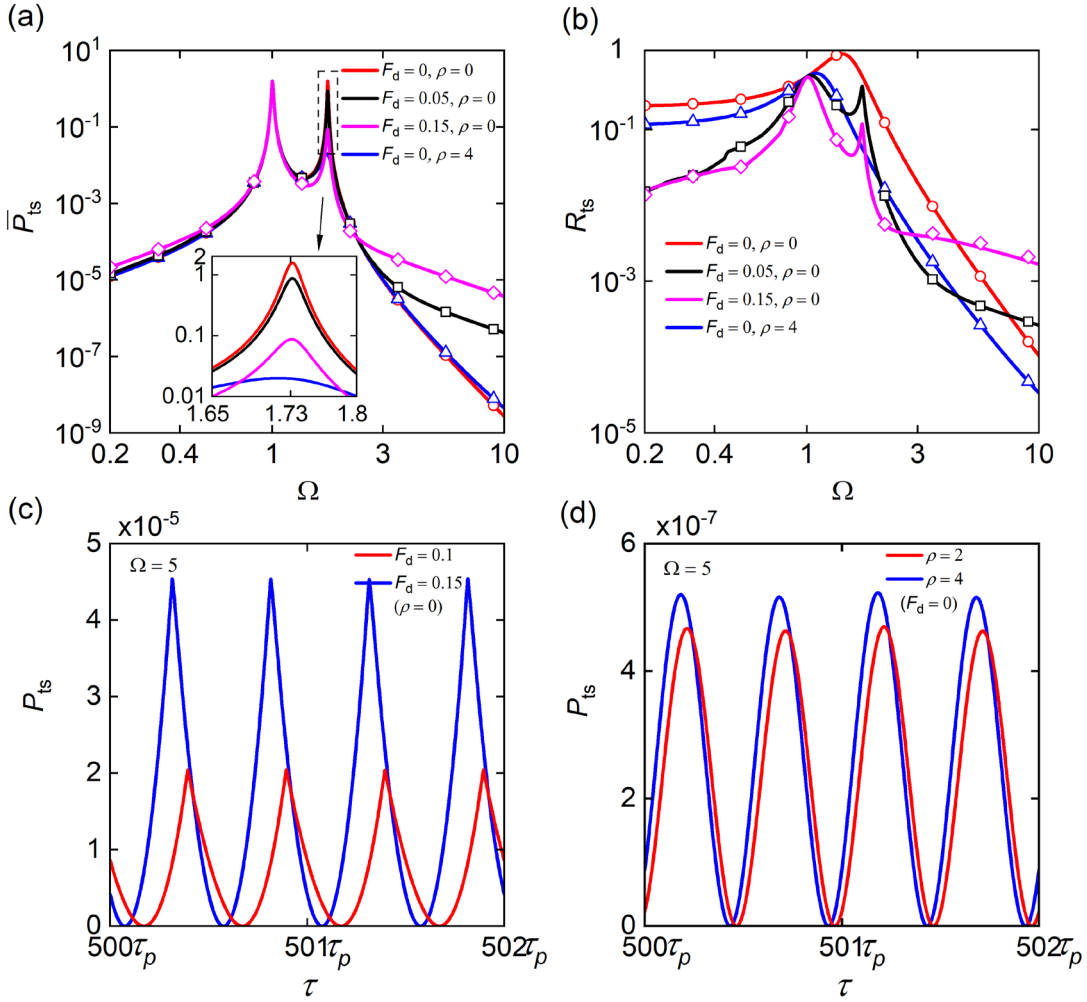

Figure 15. Effects of the interfacial friction on (a) the time-averaged transmitted power $\bar{P}_{ts}$, (b) the power transmission ratio R_{ts}, and on time histories of the instantaneous transmitted power P_{ts} at the excitation frequency of $\Omega = 5$ for (c) the frictional contact cases and for (d) the viscous damper cases, respectively. In (a) and (b), the red and blue lines are for the linear system with $\rho = 0$ and 4, respectively. The black and pink lines are for friction cases with $F_d = 0.05$ and 0.15, respectively. In (c), the red and blue lines are for friction cases with $F_d = 0.1$ and 0.15, respectively. In (d), the red and blue lines are for the linear system with $\rho = 2$ and 4, respectively. Circular, square, diamond and triangular symbols denote RK results.

With the increasing excitation frequency, the differences in the values of $\bar{P}_{ts}$ between the interfacial viscous damper case (i.e., Case 4) and the dry friction cases are enlarged, as shown in Fig. 15(a). The reason is that at high frequencies, compared to the interfacial viscous damper, the dry friction at the coupling interface can result in a larger transmitted force to the secondary system and also a larger amount of input power into the integrated system, as depicted in Figs 14(a) and (b). Therefore, there is an increasing amount of input power that is transmitted to the secondary system. Fig. 15(a) also shows that an increase in the magnitude of friction F_d from 0.05 to 0.15 can further reduce the height of the second peak of $\bar{P}_{ts}$ but increase the values of $\bar{P}_{ts}$ in the low- or high-frequency ranges. Moreover, it is noted that the interfacial friction has little influence on the first peak of $\bar{P}_{ts}$ when Ω is near the frequency of the in-phase mode of the corresponding linear system. #

To further explore the differences in the amount of the power transmission between dry friction cases and the viscous damper case in the high-frequency range, Fig. 15(c) presents the time histories of the instantaneous transmitted power P_{ts} for the dry friction cases with $F_{\mathrm{d}} = 0.1$ and 0.15 while Fig. 15(d) shows time histories of P_{ts} for the viscous damper cases with $\rho = 2$ and 4. The system is excited at $\Omega = 5$. It shows that for the dry friction cases, there is much more power transmitted to the secondary system than that of the viscous damper case. A larger magnitude of friction can lead to a significantly higher amplitude of P_{ts}, as shown in Fig. 15(c). In comparison, with the increase of damping ratio ρ, only a slight increase of the amplitude of P_{ts} can be observed. Fig. 15(b) shows that for the systems in Cases 2 or 3 with interfacial friction, two peaks exist in each curve of the power transmission ratio R_{ts}. In comparison, only one peak can be found in Case 1 for the reference linear system or Case 4 for the system with interfacial viscous damper. By comparing to the reference Case 1 with $F_{\mathrm{d}} = \rho = 0$, the interfacial dry friction in Cases 2 or 3 can lead to a much smaller portion of input power being transmitted to the secondary system in the range of approximately $\Omega < 5$. At high frequencies with $\Omega > 6$, the system with interfacial viscous damper in Case 4 has a smaller value of power transmission ratio R_{ts} than that of Case 1. In contrast, the interfacial dry friction cases have a larger value of R_{ts} compared to that of Case 1. When the magnitude of friction F_{d} increases from 0.05 to 0.15, the power transmission ratio increases when the excitation frequency Ω is high but reduced when Ω is near the second peak frequency or locates in the low-frequency range with Ω being smaller than 1.

In Figs 16(a) and (b), the effects of the interfacial friction on the time-averaged dissipated power $\bar{P}_{\mathrm{di}}$ at the interface and the corresponding power dissipation ratio R_{di} are studied. Fig. 16(a) shows that when the excitation frequency Ω is near the out-of-phase mode ($\Omega \approx 1.74$), there are relatively small difference in the values of power dissipation $\bar{P}_{\mathrm{di}}$ between systems with interfacial dry friction and the system with interfacial viscous damper. However, at low or high frequencies with Ω away from the peak frequency, there can be a much larger amount of power dissipation by the interfacial friction than that by the interfacial viscous damping. As the magnitude of friction F_{d} increases from 0.05 to 0.15, there is a slight reduction in the peak value of power dissipation $\bar{P}_{\mathrm{di}}$ but a significant increase in its values when the excitation frequency is away from the peak. Fig. 16(b) shows that for the system with interfacial viscous damper with $\rho = 4$, there is a local minimum point near the in-phase mode of the corresponding linear system in the curve of the power transmission ratio R_{di}. For the considered systems with interfacial dry friction, there is an extra local minimum point of R_{di} appearing near the out-of-phase mode of the linear system. In the low- or high-frequency ranges, the values of R_{di} for interfacial friction cases are close to 1, indicating that a large portion of the input power is dissipated at the interface. Fig. 16(b) also shows that an increase in the magnitude of friction F_{d} from 0.05 to 0.15 can increase the values of R_{di} near the frequencies of two local minimum points. By combining the curves of power transmission ratio R_{ts} shown in Fig. 15(b), it can be summarized that the interfacial frictional contact can significantly alter the energy distribution within the coupled system.

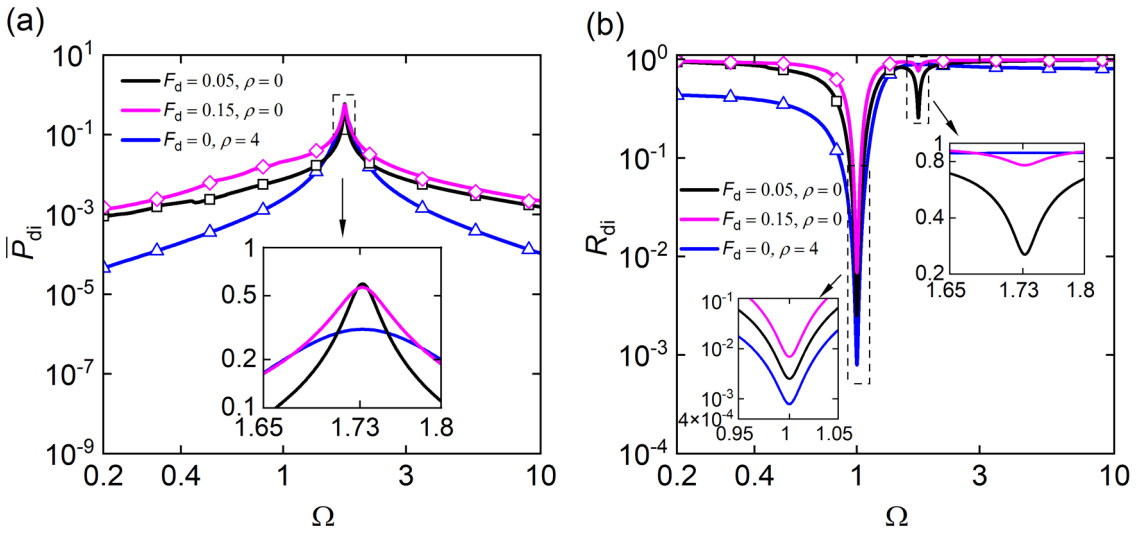

Figure 16. Effects of the magnitude of friction F_d on (a) the time-averaged dissipated power $\bar{P}_{di}$ at the interface and (b) the power dissipation ratio R_{di}, respectively. The blue line is for the frictionless linear system with $\rho = 4$. The black and pink lines are for the nonlinear system having dry friction at the interface with $F_d = 0.05$ and 0.15, respectively. Square, diamond and triangular symbols denote RK results.

In Fig. 17, the influence of the interfacial dry friction on the power dissipation is further investigated by examining the steady-state instantaneous power dissipation P_{di} at different excitation frequencies. Figs 17(a), (b) and (c) present the time histories of P_{di} considering interfacial friction with $F_d = 0.05$ or 0.15 ($\rho = 0$) while Figs 17(d), (e) and (f) show the corresponding results associated with the interfacial viscous damper case with $\rho = 2$ or 4 ($F_d = 0$) for comparison. The excitation frequency is set as 0.4 in Figs 17(a) and (c), 1.74 in Figs 17(b) and (d), and 5 in Figs 17(c) and (f). The other parameters are set the same as those used in Fig. 16. Fig. 17(a) shows that at $\Omega = 0.4$ in the low-frequency range, over a portion of an excitation cycle, there is no power dissipation by the dry frictional contact. This is because that the masses are in the stick state due to the non-smooth friction nonlinearity. As suggested by Eq. (34b), the dry friction contact cannot dissipate power in the stick state without relative motion between the masses. By comparing to the viscous damper case excited at the same frequency as shown in Fig. 17(d), it is found that the interfacial friction can lead to a much higher amplitude of P_{di} and hence a larger time-averaged power dissipation $\bar{P}_{di}$ at the interface.

In Figs 17(b) and (e), the systems are excited at $\Omega = 1.74$ near the peak frequency of $\bar{P}_{di}$ associated with the out-of-phase mode. A comparison between the subfigures shows that the interfacial friction and viscous damping can result in similar amount of power dissipation. The increase of magnitude of friction F_d can lead to a slight increase in the amplitude of power dissipation P_{di} at the interface, as shown in Fig. 17(b). In contrast, an increase of viscous damping coefficient can reduce the amplitude of P_{di}, as shown in Fig. 17(e). It is due to the smaller relative motion between two masses when there is stronger interfacial viscous damping. Figs 17(c) and (f) present the results associated with the systems excited at $\Omega = 5$ with interfacial friction or viscous damping, respectively. It shows that there is more energy dissipation by the dry friction compared to that by the interfacial viscous damper. Fig. 17

demonstrates that interfacial friction can effectively dissipate vibration energy when the system is excited at low or high frequencies.

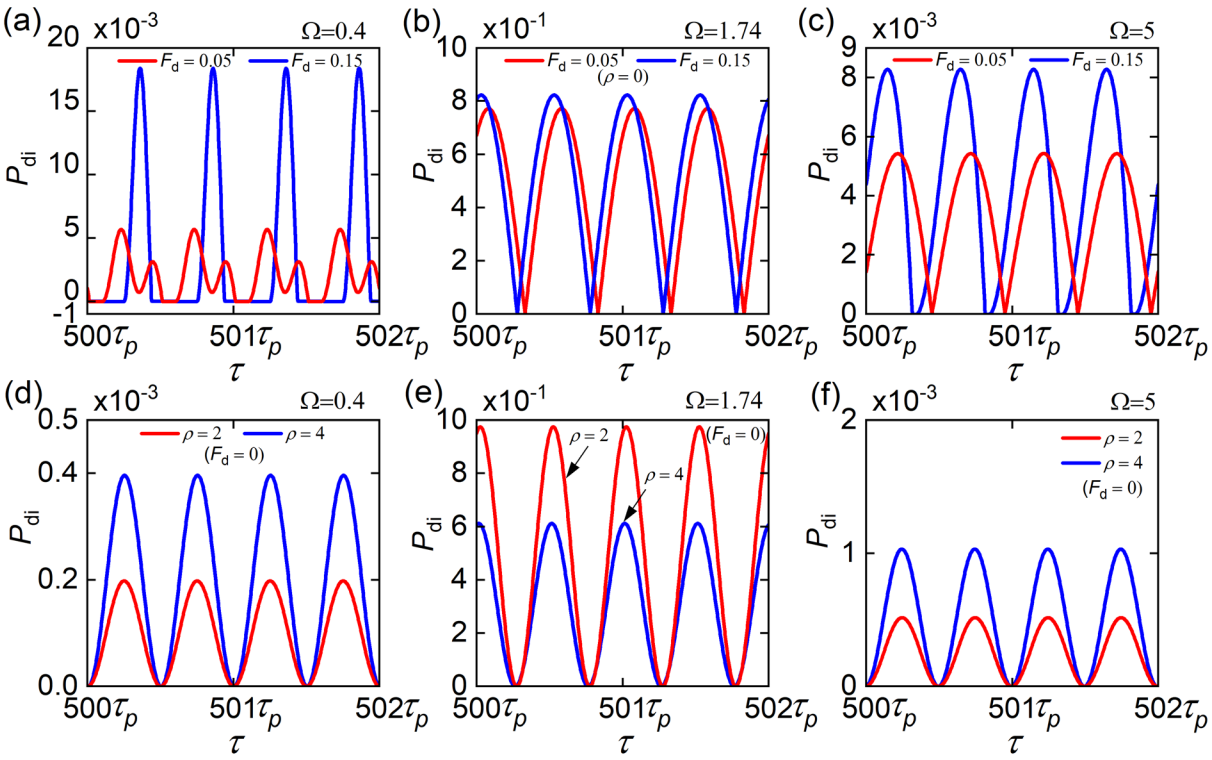

Figure 17. Instantaneous dissipated power P_{di} for the frictional contact cases in (a), (b) and (c). (d), (e) and (f) are for the viscous damper cases. The systems are excited at $\Omega = 0.4$ in (a) and (c), at $\Omega = 1.74$ in (b) and (e), and at $\Omega = 5$ in (c) and (f). In (a), (b) and (c), the red and blue lines are for frictional cases with $F_{\mathrm{d}} = 0.05$ and 0.15, respectively. In (d), (e) and (f), the red and blue lines are for viscous damper cases with $\rho = 2$ and 4, respectively.

5 Conclusions

This study is focussed on the vibration transmission and energy dissipation in systems with Comloub frictional contact. A general energy flow analysis framework for systems with friction has been presented and was applied to study a forced SDOF system and a coupled system with interfacial frictional contact. Both the Karnopp discontinuous model and smooth Coulomb friction models were used in the HB approximations and direct numerical integration. The effects of having frictional contact on the vibration transmission and energy dissipation within the SDOF and 2DOF systems were evaluated quantitatively by the force transmissibility and time-averaged power flow variables.

For the SDOF system with frictional contact, it was shown that the friction can effectively suppress the dynamic response when the excitation frequency locates in the low- or high-frequency ranges away from the resonance. It can remarkably increase the force transmission and the time-averaged input power into the system in these frequency ranges. The existence of the frictional contact in the system can reduce the maximum kinetic energy at high frequencies but can increase its value in the low-frequency range. Moreover, the change of the magnitude of dynamic dry friction force can significantly affect the energy flow characteristics at frequencies away from the resonance.

For the coupled system with dry friction at the contacting interface, it was shown that the interfacial dry friction can suppress the motion of the system excited at the out-of-phase mode but can considerably increase the response amplitude of the secondary mass at high frequencies. In the high-frequency range, the presence of the frictional contact can lead to larger force transmissibility to the secondary system, and a larger amount of the time-averaged transmitted power from the force-excited system, through the interface to the secondary system. Moreover, a higher level of friction can lead to more substantial increases in the energy dissipation at the interface in the low or high-frequency ranges, compared to the influence of increasing interfacial viscous damping. The energy distribution within the coupled system can be tuned by the interfacial frictional contact. The study demonstrated that frictional contact within dynamical systems can be properly designed to achieve desirable vibration energy flow transmission and dissipation behaviour for better dynamic performance.

Acknowledgements

This work was supported by National Natural Science Foundation of China [Grant number 51605233] and by Ningbo Municipal Bureau of Science and Technology under Natural Science Programme [Grant number 2019A610155].

References

[1] Tian Q, Flores P, Lankarani HM. A comprehensive survey of the analytical, numerical and experimental methodologies for dynamics of multibody mechanical systems with clearance or imperfect joints. Mech Mach Theory 2018;122:1-57.

[2] Xie D, Huang Z, Ma Y, Vaziri V, Kapitaniak M, Wiercigroch M. Nonlinear dynamics of lump mass model of drill-string in horizontal well. Int J Mech Sci 2020;174:105450.

[3] Mercier A, Jézéquel L, Besset S, Hamdi A, Diebold J-F, Studies on detachment non-linearity at the rotor-stator interface. J Sound Vib 2020;468:115084.

[4] Bao H, Huang W, Lu F. Investigation of engagement characteristics of a multi-disc wet friction clutch. Tribol Int 2021;159:106940.

[5] Mostaghel N. A non-standard analysis approach to systems involving friction. J Sound Vib 2005;284:583-595.

[6] Liu Y, Pavlovskaia E, Hendry D, Wiercigroch M. Vibro-impact responses of capsule system with various friction models. Int J Mech Sci 2013;72:39-54.

[7] Yan Y, Liu G, Wiercigroch M, Xu J. Safety estimation for a new model of regenerative and frictional cutting dynamics. Int J Mech Sci 2021;201:106468.

[8] Rusinek R, Wiercigroch M, Wahi P. Modelling of frictional chatter in metal cutting. Int J Mech Sci 2014;89:167-176.

[9] Marques F, Flores P, Pimenta Claro JC, Lankarani HM. A survey and comparison of several friction force models for dynamic analysis of multibody mechanical systems. Nonlinear Dyn 2016;86:1407-1443.

[10] Jaisee S, Yue F, Ooi YH. A state-of-the-art review on passive friction dampers and their applications. Eng Struct 2021;235:112022.

[11] Gaul L, Nitsche R. The role of friction in mechanical joints. Appl Mech Rev 2001;54:93-106.

[12] Hartog JPD. Forced vibrations with combined viscous and Coulomb damping. Trans Am Soc Mech Eng 1930;9:801-817.

[13] Hundal MS. Response of a base excited system with Coulomb and viscous friction. J Sound Vib 1979;64:371-378.

[14] Marui E, Kato S. Forced vibration of a base-excited single-degree-of-freedom system with coulomb friction. J Dyn Syst-T ASME 1984;106:280-285.

[15] Marino L, Cicirello A. Experimental investigation of a single-degree-of-freedom system with Coulomb friction. Nonlinear Dyn 2020;99:1781-1799.

[16] Saha A, Wiercigroch M, Jankowski K, Wahi P, Stefański A. Investigation of two different friction models from the perspective of friction-induced vibrations. Tribol Int 2015;90:185-197.

[17] Jin X, Xu H, Wang Y, Huang Z. Approximately analytical procedure to evaluate random stick-slip vibration of Duffing system including dry friction. J Sound Vib 2019;443:520-536.

[18] Awrejcewicz J, Olejnik P. Stick-slip dynamics of a two-degree-of-freedom system. Int J Bifurcat Chaos 2003;13:843-861.

[19] Wang XC, Huang B, Wang RL, Mo JL, Ouyang H. Friction-induced stick-slip vibration and its experimental validation. Mech Syst Signal Process 2020;142:106705.

[20] Shaw SW. On the dynamic response of a system with dry friction. J Sound Vib 1986;108:305-325.

[21] Feeny B. A nonsmooth coulomb friction oscillator. Physica D 1992;59:25-38.

[22] Feeny B, Moon FC, Chaos in a forced dry-friction oscillator: experiments and numerical modelling. J Sound Vib 1994;170:303-323.

[23] Hong HK, Liu CS. Coulomb friction oscillator: modelling and responses to harmonic loads and base excitations. J Sound Vib 2000;229:1171-1192.

[24] Luo ACJ, Gegg BC. Stick and non-stick periodic motions in periodically forced oscillators with dry friction. J Sound Vib 2006;291:132-168.

[25] Oancea VG, Laursen TA. Investigations of low frequency stick–slip motion: experiments and numerical modelling. J Sound Vib 1998;213:577-600.

[26] Duan C, Singh R. Influence of harmonically varying normal load on steady-state behavior of a 2dof torsional system with dry friction. J Sound Vib 2006;294:503-528.

[27] Papangelo A, Ciavarella M. On the limits of quasi-static analysis for a simple Coulomb frictional oscillator in response to harmonic loads. J Sound Vib 2015;339:280-289.

[28] Pascal M. Sticking and nonsticking orbits for a two-degree-of-freedom oscillator excited by dry friction and harmonic loading. Nonlinear Dyn 2014;77:267-276.

[29] Sun Y, Vizzaccaro A, Yuan J, Salles L. An extended energy balance method for resonance prediction in forced response of systems with non-conservative nonlinearities using damped nonlinear normal mode. Nonlinear Dyn 2020;103:3315-3333.

[30] Wiercigroch M, Sin VWT, Liew ZFK. Non-reversible dry friction oscillator: design and measurements. Proc Inst Mech Eng 1999;213:527–534.

[31] Wojewoda J, Stefański A, Wiercigroch M, Kapitaniak T. Hysteretic effects of dry friction: modelling and experimental studies. Philos Trans R Soc Lond Ser A Math Phys Eng Sci 2008;366:747-765.

[32] Kapitaniak M, Vaziri Hamaneh V, Páez Chávez J, Nandakumar K, Wiercigroch M. Unveiling complexity of drill–string vibrations: Experiments and modelling. Int J Mech Sci 2015;101-102:324-337.

[33] Bhaskararao AV, Jangid RS. Harmonic response of adjacent structures connected with a friction damper. J Sound Vib 2006;292:710-725.

976 [34] Krack M, Bergman LA, Vakakis AF. On the efficacy of friction damping in the presence of nonlinear
977 modal interactions. J Sound Vib 2016;370:209-220.

978 [35] Szwedowicz J, Gibert C, Sommer TP, Kellerer R. Numerical and experimental damping assessment of
979 a thin-walled friction damper in the rotating setup with high pressure turbine blades. J Eng Gas Turb
980 Power 2008;130.

981 [36] Stammers CW, Sireteanu T. Vibration control of machines by use of semi-active dry friction damping.
982 J Sound Vib 1998;209:671-684.

983 [37] Sorge F. Damping of rotor conical whirl by asymmetric dry friction suspension. J Sound Vib
984 2009;321:79-103.

985 [38] Petrov EP, Ewins DJ. Analytical formulation of friction interface elements for analysis of nonlinear
986 multi-harmonic vibrations of bladed disks. J Turbomach 2003;125:364-371.

987 [39] Krack M, Salles L, Thouverez F. Vibration prediction of bladed disks coupled by friction joints. Arch
988 Comput Method E 2017;24:589-636.

989 [40] Claeys M, Sinou JJ, Lambelin JP, Todeschini R. Experiments and numerical simulations of nonlinear
990 vibration responses of an assembly with friction joints – Application on a test structure named
991 "Harmony". Mech Syst Signal Process 2016;70-71:1097-1116.

992 [41] Donmez A, Cigeroglu E, Ozgen GO. An improved quasi-zero stiffness vibration isolation system
993 utilizing dry friction damping. Nonlinear Dyn 2020;101:107-121.

994 [42] Levitan ES. Forced oscillation of a spring-mass system having combined coulomb and viscous
995 damping. J Acoust Soc Am 1960;32:1265-1269.

996 [43] Marino L, Cicirello A, Hills DA. Displacement transmissibility of a Coulomb friction oscillator subject
997 to joined base-wall motion. Nonlinear Dyn 2019;98:2595-2612.

998 [44] Ciğeroğlu E, Özgüven HN. Nonlinear vibration analysis of bladed disks with dry friction dampers. J
999 Sound Vib 2006;295:1028-1043.

1000 [45] López I, Busturia JM, Nijmeijer H. Energy dissipation of a friction damper. J Sound Vib 2004;278:539-
1001 561.

1002 [46] Lopez I, Nijmeijer H. Prediction and validation of the energy dissipation of a friction damper. J Sound
1003 Vib 2009;328:396-410.

1004 [47] Nicolas M. A comprehensive study on the behavior of a rigid block on an oscillating ground with
1005 friction, elastic and viscous forces. Int J Nonlin Mech 2017;93:21-29.

1006 [48] Do N, Ferri AA. Energy transfer and dissipation in a three-degree-of-freedom system with stribeck
1007 friction. in: ASME 2005 International Mechanical Engineering Congress and Exposition, 2005, pp.
1008 195-204.

1009 [49] Goyder HGD, White RG. Vibrational power flow from machines into built-up structures. J Sound Vib
1010 1980;68:59-117.

1011 [50] Xiong YP, Xing JT, Price WG. A general linear mathematical model of power flow analysis and control
1012 for integrated structure–control systems. J Sound Vib 2003;267:301–34.

1013 [51] Zhu C, Yang J, Rudd C. Vibration transmission and power flow of laminated composite plates with
1014 inerter-based suppression configurations. Int J Mech Sci 2021;190:106012.

1015 [52] Yang J, Xiong YP, Xing JT. Nonlinear power flow analysis of the Duffing oscillator. Mech Syst Signal
1016 Process 2014;45:563–78.

1017 [53] Yang J, Xiong YP, Xing JT. Power flow behaviour and dynamic performance of a nonlinear vibration
1018 absorber coupled to a nonlinear oscillator. Nonlinear Dyn 2015;80:1063–79.

1019 [54] Yang J, Xiong YP, Xing JT. Dynamics and power flow behaviour of a nonlinear vibration isolation
1020 system with a negative stiffness mechanism. J Sound Vib 2013;332:167–83.

[55] Yang J, Xiong YP, Xing JT. Vibration power flow and force transmission behaviour of a nonlinear isolator mounted on a nonlinear base. Int J Mech Sci 2016;115-116:238–52.

[56] Yang J, Jiang JZ, Neild SA. Dynamic analysis and performance evaluation of nonlinear inerter-based vibration isolators. Nonlinear Dyn 2019;99:1823-1839.

[57] Yang J, Shi B, Rudd C. On vibration transmission between interactive oscillators with nonlinear coupling interface. Int J Mech Sci 2018;137:238-251.

[58] Shi B, Yang J, Rudd C. On vibration transmission in oscillating systems incorporating bilinear stiffness and damping elements. Int J Mech Sci 2019;150:458-470.

[59] Dai W, Yang J, Shi B. Vibration transmission and power flow in impact oscillators with linear and nonlinear constraints. Int J Mech Sci 2020;168:105234.

[60] Dai W, Yang J. Vibration transmission and energy flow of impact oscillators with nonlinear motion constraints created by diamond-shaped linkage mechanism. Int J Mech Sci 2021;194:106212.

[61] Karnopp D. Computer simulation of stick-slip friction in mechanical dynamic systems. J Dyn Syst-T ASME 1985;107:100-103.

[62] Pennestrì E, Rossi V, Salvini P, Valentini PP. Review and comparison of dry friction force models. Nonlinear Dyn 2016;83:1785-1801.

[63] Mostaghel N, Davis T. Representations of coulomb friction for dynamic analysis. Earthq Eng Struct D 1997;26:541-548.

[64] Stein GJ, Zahoranský R, Múčka P. On dry friction modelling and simulation in kinematically excited oscillatory systems. J Sound Vib 2008;311:74-96.

[65] Yuan T-C, Yang J, Chen L-Q. A harmonic balance approach with alternating frequency/time domain progress for piezoelectric mechanical systems. Mech Syst Signal Process 2019;120:274-289.

[66] Von Groll G, Ewins DJ. The harmonic balance method with arc-length continuation in rotor/stator contact problems. J Sound Vib 2001;241:223-233.